Table of Contents

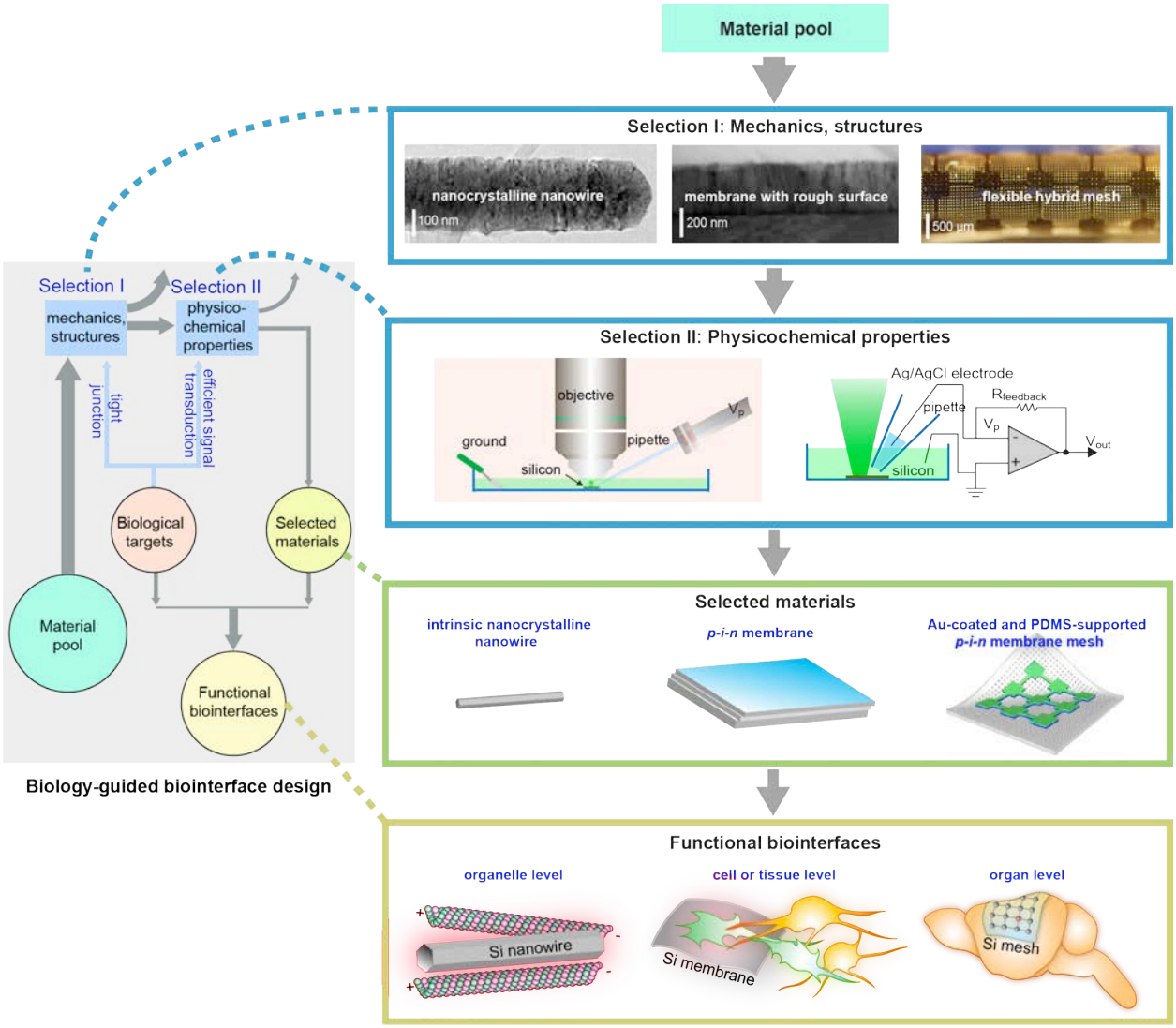

Supplementary Figure 1 | A schematic diagram illustrating the organization of the entire paper. In this work, we focused on the rational design of Si structures for optically-controlled biointerfaces and formulated a biology-guided design principle that is based on the structures and mechanics (**Selection I**) and the photo-responses (**Selection II**) of various Si materials. The **Selection I** yields nanocrystalline nanowires (for the organelle level interface), membranes with rough surfaces (for the cell and tissue level interface), and flexible and distributed meshes (for the organ level interface) for tight interfaces. **Selection II** examines the effects of other orthogonal controls of Si (*e.g.,* size, doping, surface chemistry) for desirable physicochemical signal transductions at the biointerfaces. These two **Selections** highlight nano-confinement-enabled thermal responses from nanocrystalline nanowires, *p-i-n* diode junction-enhanced

capacitive currents, and metal-enhanced capacitive and Faradaic currents, all in freestanding configurations (**Selected materials**). In consideration of the materials structures, mechanics, and photo-responses, we focused on the intrinsic nanocrystalline Si nanowires for intracellular and the related intercellular probing, and only used the photothermal effect. For single cell or small tissue level inter- and extracellular studies, we primarily explored a light-induced capacitive effect, *i.e.,* we used a *p-i-n* Si multilayered membrane where the biological invasiveness from capacitive electrochemical currents are usually minimal. Finally, given that the organ level modulation would require the largest stimuli, we used the Au-coated Si *p-i-n* membranes for *in vivo* studies (**Functional biointerfaces**).

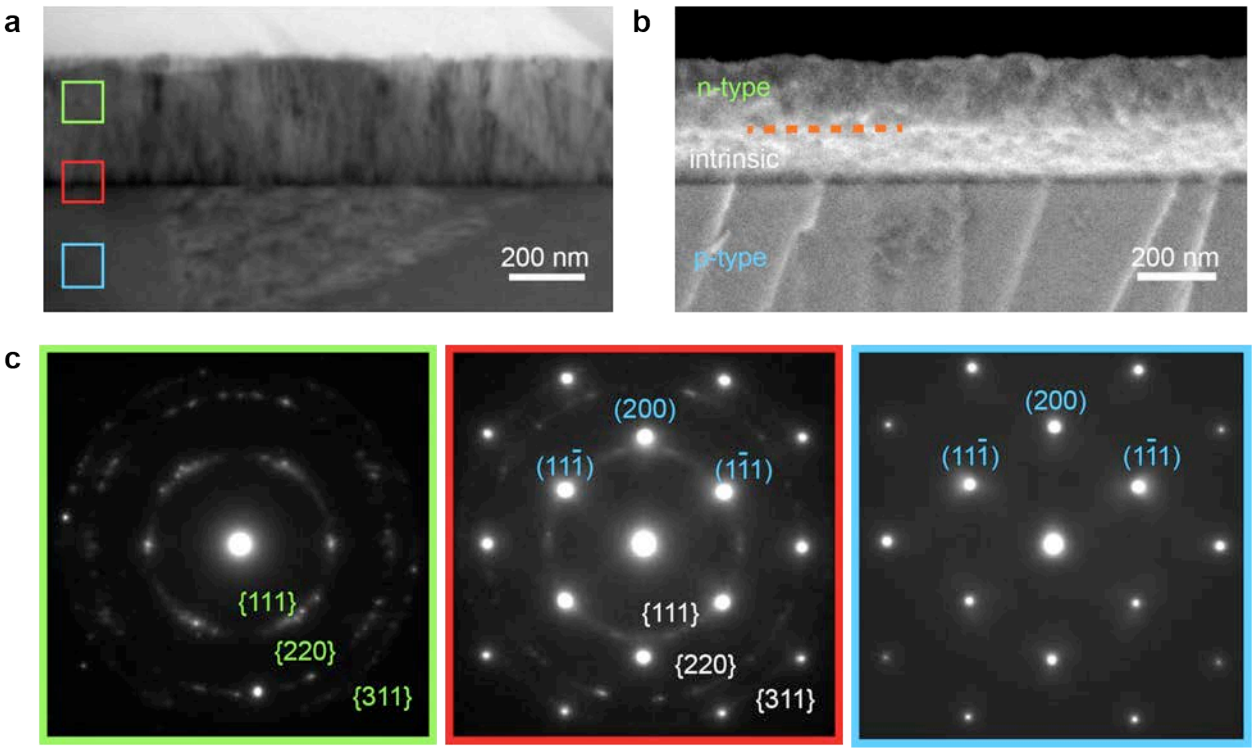

Supplementary Figure 2 | Cross-sectional views of the *p-i-n* Si diode junction. a, A TEM image showing the columnar structure of the intrinsic and *n*-type layers grown on the *p*-type substrate. Colored boxes (green, *n*-type Si; red, *p*-type/intrinsic interface; blue, *p*-type Si) denote the regions for SAED in **c**. **b,** A SEM image showing the thicknesses of both the intrinsic (white) and *n*-type layers (green). To enhance the SEM contrast for each layer, the sample was prepared by etching of a *p-i-n* diode junction in a 20% (w/v) potassium hydroxide (KOH) aqueous solution at 60 ^{o}C for 10 s. The orange dashed line highlights the intrinsic/*n*-type interface. **c,** SAED patterns taken from the [011] zone axis showing the crystallinity transition from a [100]-oriented single crystalline *p*-type substrate (isolated spots with blue labels) to nanocrystalline intrinsic (concentric rings with white labels) and *n*-type (concentric rings with green labels) layers with grain boundaries roughly aligned with the [100] direction.

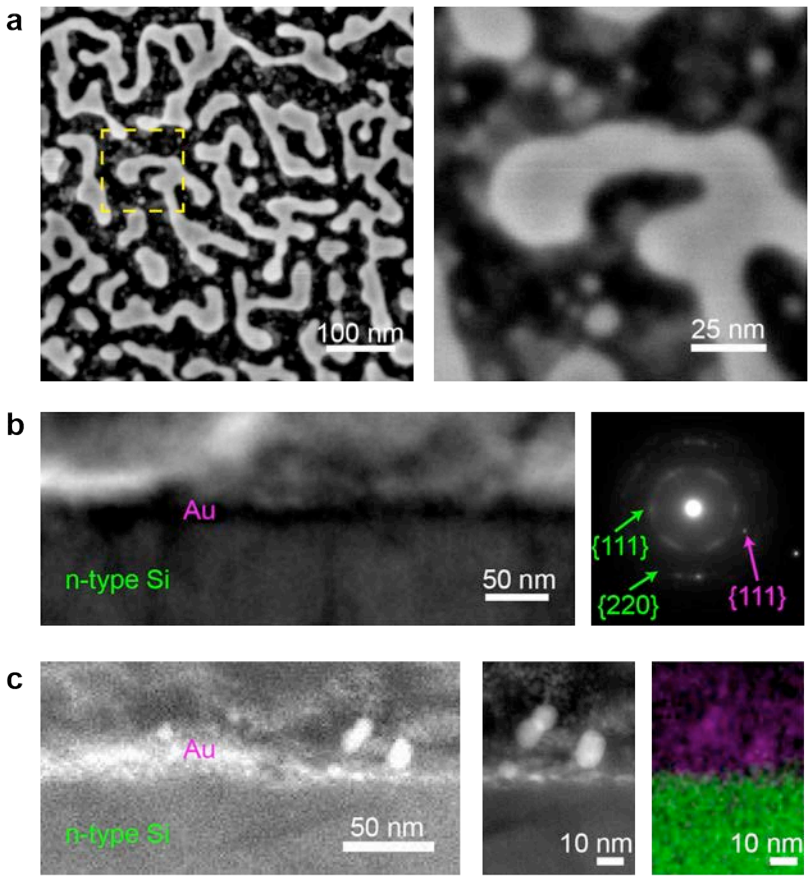

Supplementary Figure 3 | Structural characterizations of gold-decorated *p-i-n* membrane. **a,** Top-view SEM images showing the interconnected meshes made of gold. The yellow box in the left image highlights the region for a zoom-in view (right) and shows the coexistence of small nanoparticles together with the large meshes. **b,** A cross-sectional bright field TEM image (left) taken at the Au-Si interface where Au appears to be dark. A SAED pattern (right) shows the diffraction features from both Si and Au. **c,** A high-angle annular dark field (HAADF) STEM image (left) taken at the Au-Si interface where Au has a higher contrast than Si. A zoom-in view (middle) and its corresponding XEDS map (right, purple, Au M series; green, Si K series) highlight the sharp interface.

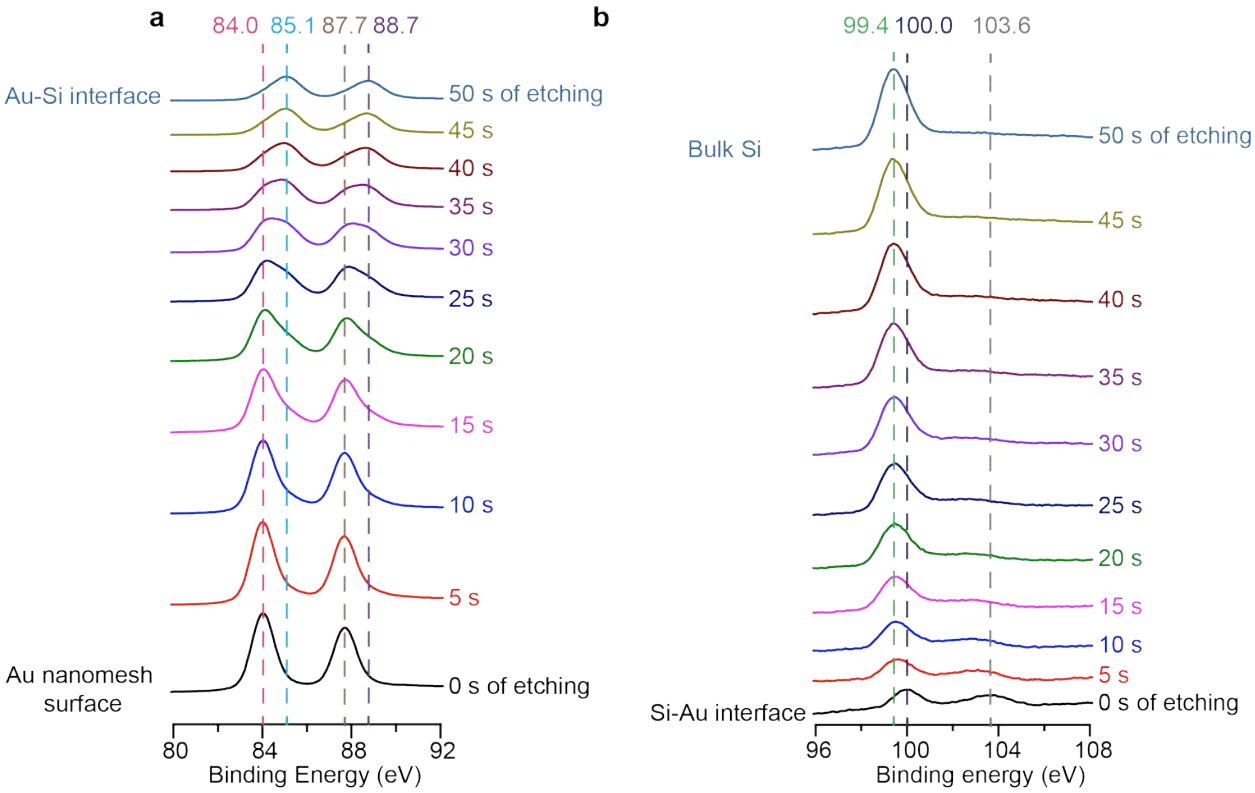

Supplementary Figure 4 | XPS depth profiles suggest the formation of Au-Si bonds at the interface. a, XPS spectra of Au taken at different depths from the surface of Au nanoparticles/nanomeshes to the interface between Au and Si. Controlled argon (Ar) plasma etching was employed to provide the depth profiles. The shift of binding energy peaks from metallic Au (84.0 eV of 4*f* 7/2 and 87.7 eV of 4*f* 5/2) to intermetallic Au (85.1 eV of 4*f* 7/2 and 88.7 eV of 4*f* 5/2) indicates the existence of Au-Si bonds at the interface. **b,** XPS spectra of Si taken at different depths from the interface between Au and Si to the bulk Si. The facts that the Si^{4+} 2*p* peak at 103.6 eV diminishes and the Si^{0} 2*p* peak shifts from 100 eV to 99.4 eV as Si is being etched both suggest the existence of oxidized form of Si at the Au-Si interface.

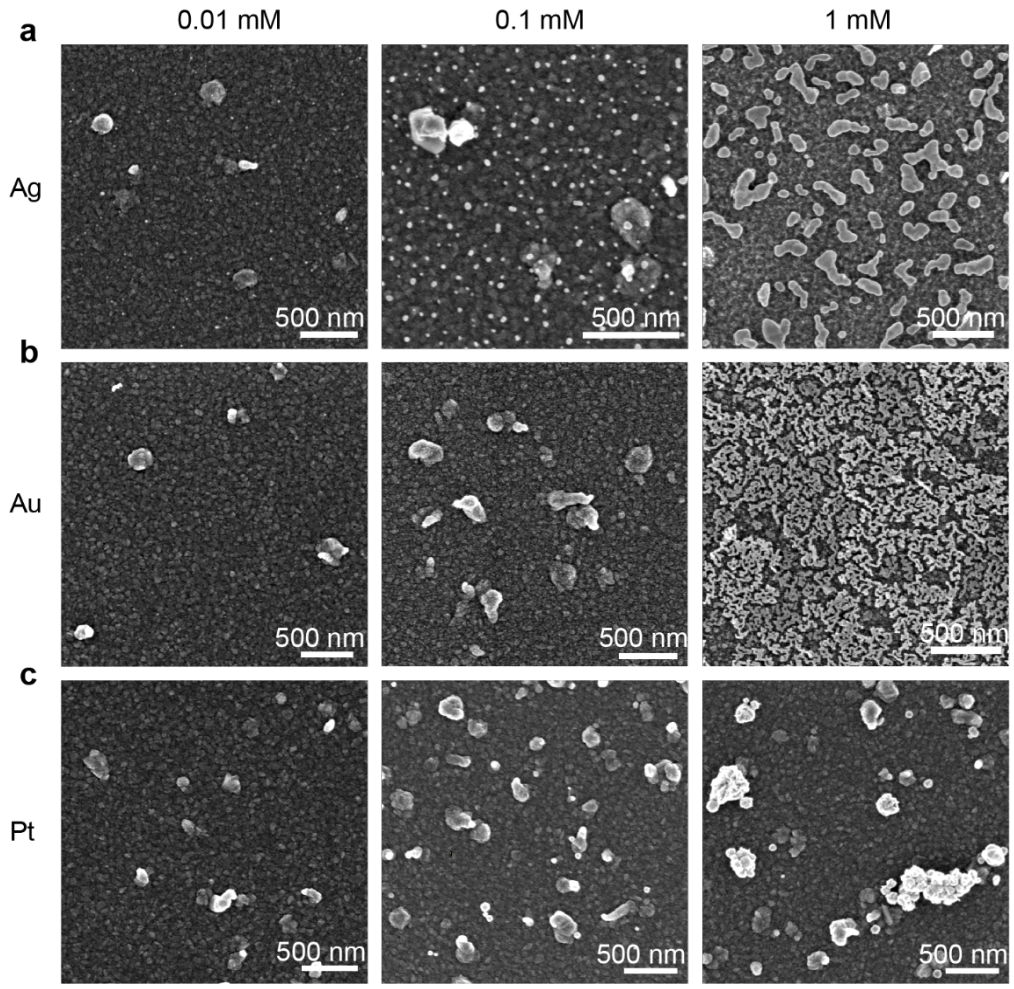

Supplementary Figure 5 | SEM images of various metal-decorated *p-i-n* membranes (Ag, Au, and Pt) prepared from aqueous precursors of different concentrations (0.01, 0.1 and 1 mM of $AgNO_3$, $HAuCl_4$ and K_2PtCl_4). In general, higher concentrations of precursors lead to higher surface coverage of metals and/or larger particle sizes.

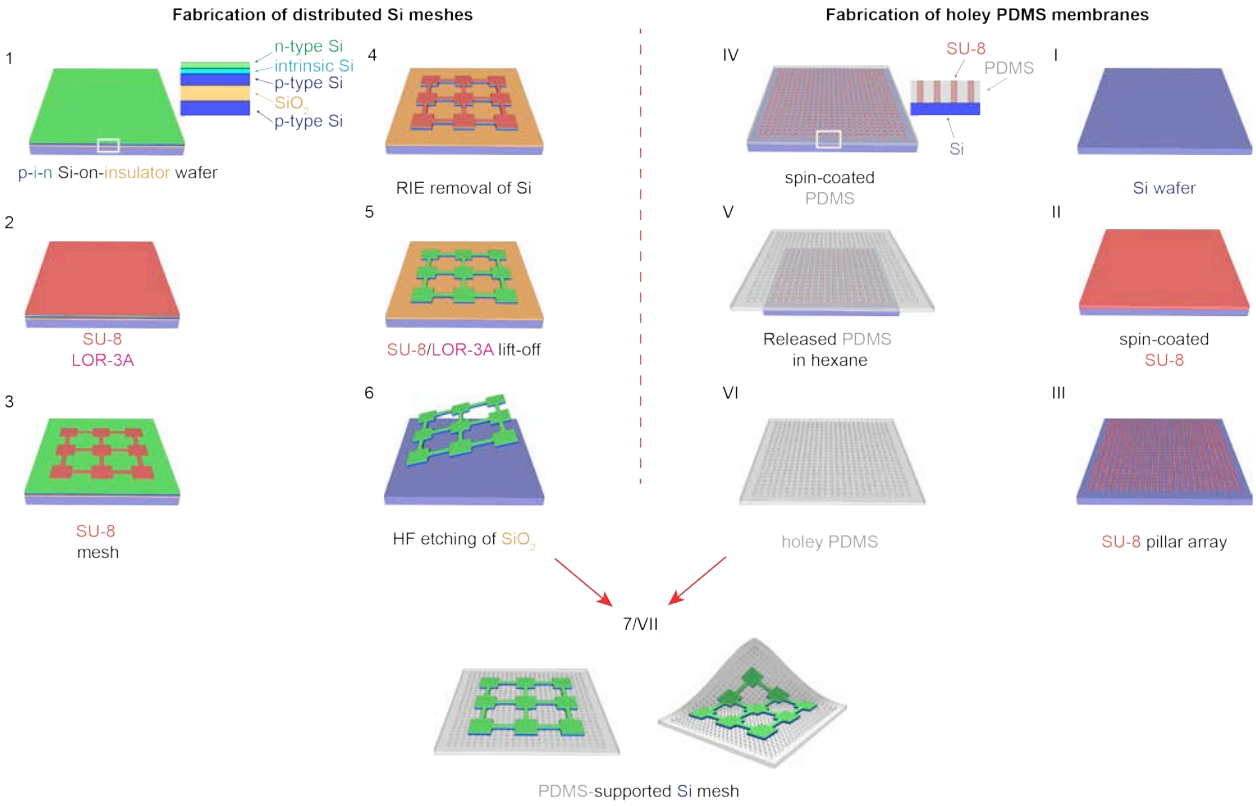

Supplementary Figure 6 | Schematic diagrams illustrating the fabrication procedures of the flexible device made of PDMS and Si. (1-6) Fabrication of the distributed Si mesh by a combination of photolithography, reactive ion etching, and wet etching processes. (I-VI) Fabrication of the holey PDMS membrane with the soft lithography technique. (7/VII) Transfer of the Si mesh onto the PDMS membrane for the final device.

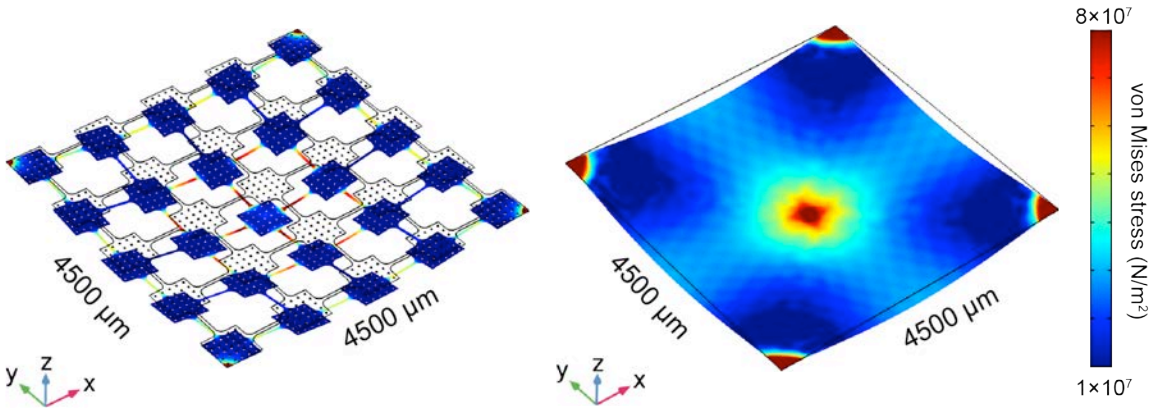

Supplementary Figure 7 | A distributed Si mesh mitigates stress over a large area. Finite element analysis of the *von Mises* stress distributions in a distributed Si mesh (left) and a solid Si membrane (right) upon indentation. The Si mesh with a holey structure shows a more uniform stress distribution across individual Si pads, suggesting a potentially more consistent optical stimulation performance in different locations. For solid Si membrane, a large stress variation was observed, suggesting performance heterogeneity. Additionally, the relaxed stress in the distributed mesh suggests a better mechanical stability during the device assembly and operation.

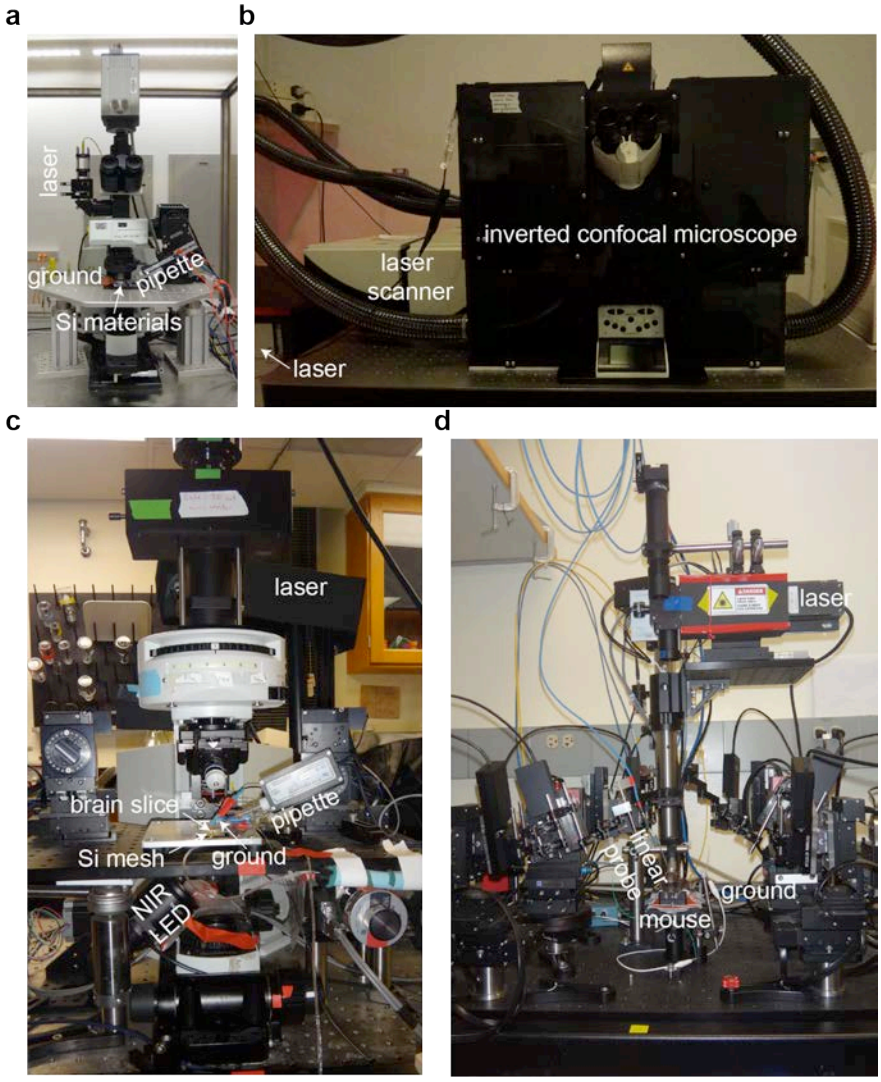

Supplementary Figure 8 | Photographs of experimental setups. a, Photo-response measurements were performed on an upright microscope equipped with a patch-clamp setup and additional light sources of a green laser and a green LED. **b**, Intra- and extracellular photostimulation experiments were done using a commercial inverted confocal microscope. The stimulation protocols were conducted in the photo-bleach module. **c**, Brain slice photostimulation experiments were conducted on an upright microscope with a patch clamp setup, equipped with near infrared (NIR) illumination for patching and a blue laser for stimulation. **d**, *In vivo* photostimulation was carried out on a custom-built apparatus combining a laser scanning system for photostimulation and an electrophysiological recording system using linear array electrodes.

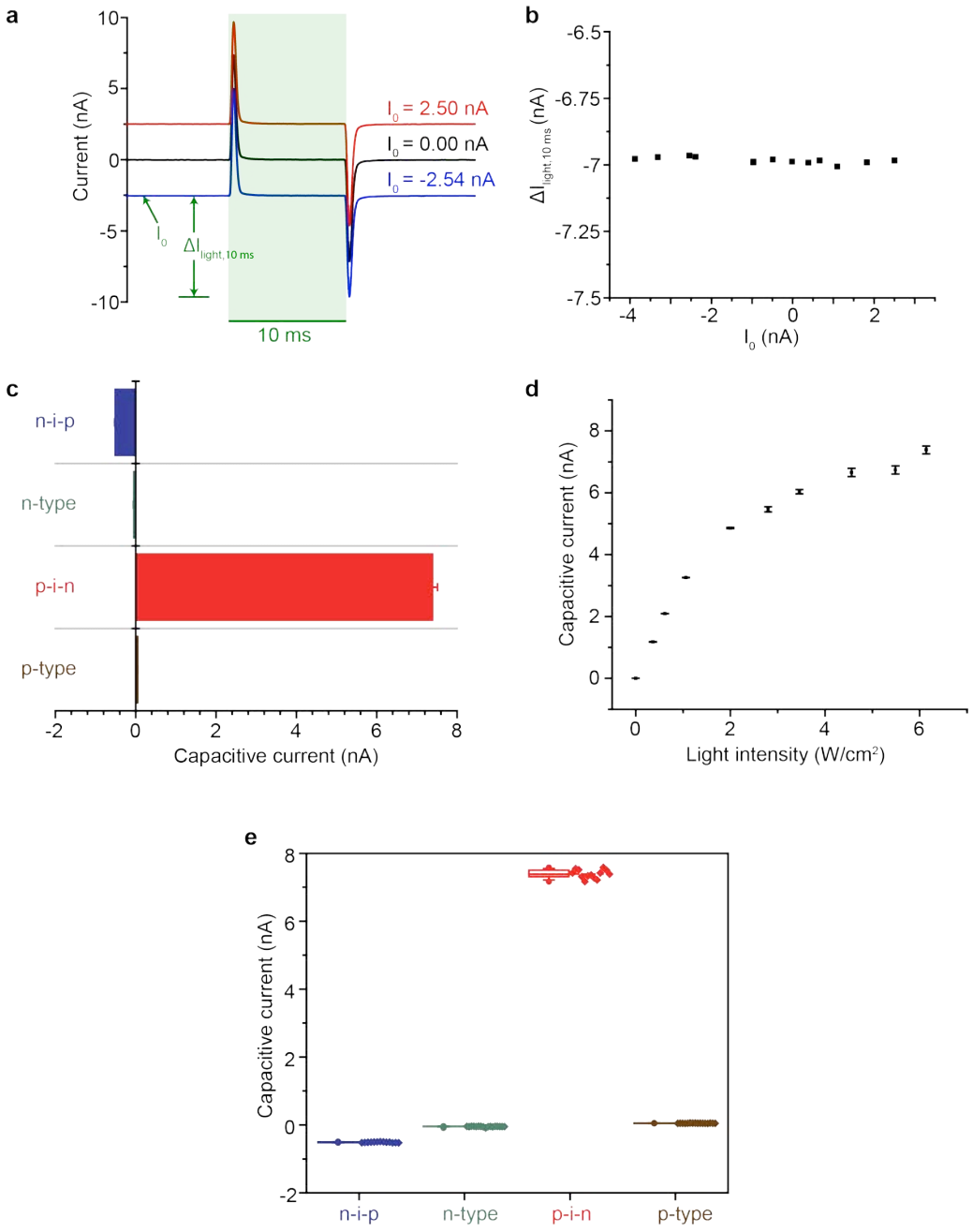

Supplementary Figure 9 | Photo-responses of dopant modulated Si structures. a, Representative current traces recorded from a *p-i-n* diode junction under LED pulses (530 nm, 10 ms, ~ 12.05 mW, ~ 500 μm spot size, ~ 6 W/cm^2), showing strong capacitive currents and minimal Faradaic currents. I_0 is defined as the baseline holding level before the light illumination. $\Delta I_{\text{lgiht,10 ms}}$ is defined as the maximal relative current amplitude after 10 ms of light illumination with respect to I_0. The light green shaded area marks the light illumination period. **b,**

The $\Delta I_{\text{light,10 ms}}$ - I_0 plot shows a negligible slope and a prominent intercept indicating strong photoelectric and weak photothermal responses. **c,** Statistical analyses of capacitive currents from different types of Si structures highlight the importance of dopant modulations. Both *p*-*i*-*n* and *n*-*i*-*p* diode junctions show significantly enhanced capacitive currents comparing to uniformly doped *p*-type and *n*-type Si. The polarities of the capacitive currents are opposite for Si with reversed doping profiles. Error bars denote standard deviations from the means. n=13 for *n*-*i*-*p*, n=17 for *n*-type, n=13 for *p*-*i*-*n*, n=16 for *p*-type. Data are from recordings at different holding levels of one representative sample for each Si structure. **d,** The amplitude for the capacitive current of a *p*-*i*-*n* diode junction can be monotonically tuned by the light intensity. Error bars denote standard deviations from the means. n=11 for the 0.36 W/cm^2 data point, n=12 for 0.62 W/cm^2, n=12 for 1.06 W/cm^2, n=12 for 2.00 W/cm^2, n=10 for 2.80 W/cm^2, n=12 for 3.46 W/cm^2, n=13 for 4.56 W/cm^2, n=11 for 5.49 W/cm^2, n=13 for 6.14 W/cm^2. **e,** Box-and-whisker plots and raw data points of the capacitive currents as shown in **c**. Half of the data points are within the boxes, 80% are within the whiskers. Solid and dashed lines represent the medians and means, respectively. Round dots mark the maximum and minimum values. Diamond dots represent the raw data points. Data are from recordings at different holding levels of one representative sample for each Si structure. n=13 for *n*-*i*-*p*, n=17 for *n*-type, n=13 for *p*-*i*-*n*, n=16 for *p*-type.

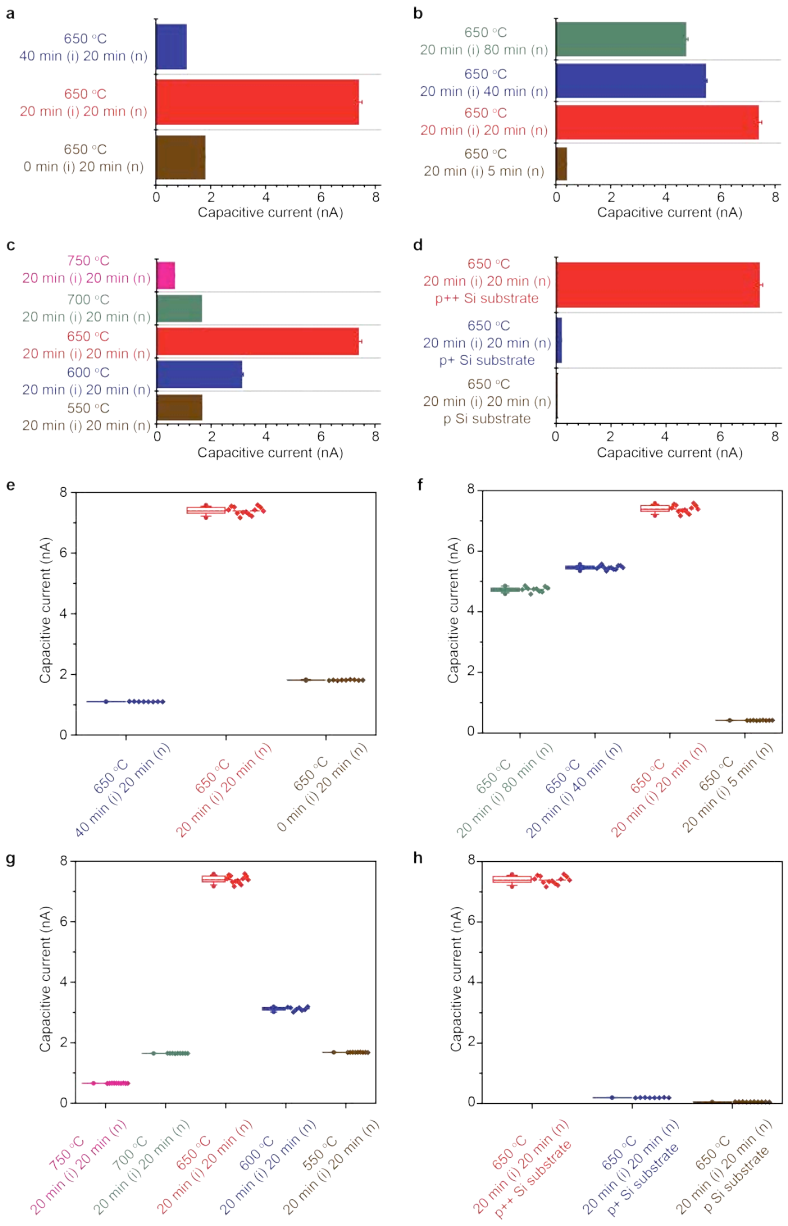

Supplementary Figure 10 | Growth optimization for the *p-i-n* multilayered membrane. Systematic studies of the intrinsic (**a**) and the *n*-type layer (**b**) deposition time and the growth temperature (**c**) indicate that an optimal value of the capacitive current can be achieved with a deposition temperature of 650 ^{o}C and a duration of 20 min for each of the intrinsic and the *n*-type layers. **d,** A heavily-doped p^{++} Si substrate, rather than p^{+} or *p* substrates, yields a higher capacitive current after the formation of a *p-i-n* diode junction. Error bars (**a-d**) denote standard deviations from the means. **e-h**, Box-and-whisker plots and raw data points of the capacitive currents as shown in **a-d**. Half of the data points are within the boxes, 80% are within the

whiskers. Solid and dashed lines represent the medians and means, respectively. Round dots mark the maximum and minimum values. Diamond dots represent the raw data points. Data are from recordings at different holding levels of one representative sample for each Si structure. In **a** and **e**, *n*=8 for 650 ^{o}C 40 min (*i*) 20 min (*n*), *n*=13 for 650 ^{o}C 20 min (*i*) 20 min (*n*), *n*=9 for 650 ^{o}C 0 min (*i*) 20 min (*n*). In **b** and **f**, *n*=10 for 650 ^{o}C 20 min (*i*) 80 min (*n*), *n*=12 for 650 ^{o}C 20 min (*i*) 40 min (*n*), *n*=13 for 650 ^{o}C 20 min (*i*) 20 min (*n*), *n*=9 for 650 ^{o}C 20 min (*i*) 5 min (*n*). In **c** and **g**, *n*=10 for 750 ^{o}C 20 min (*i*) 20 min (*n*), *n*=9 for 700 ^{o}C 20 min (*i*) 20 min (*n*), *n*=13 for 650 ^{o}C 20 min (*i*) 20 min (*n*), *n*=8 for 600 ^{o}C 20 min (*i*) 20 min (*n*), *n*=9 for 550 ^{o}C 20 min (*i*) 20 min (*n*). In **d** and **h**, *n*=13 for 650 ^{o}C 20 min (*i*) 20 min (*n*) *p*++ Si substrate, *n*=8 for 650 ^{o}C 20 min (*i*) 20 min (*n*) *p*+ Si substrate, *n*=10 for 650 ^{o}C 20 min (*i*) 20 min (*n*) *p* Si substrate.

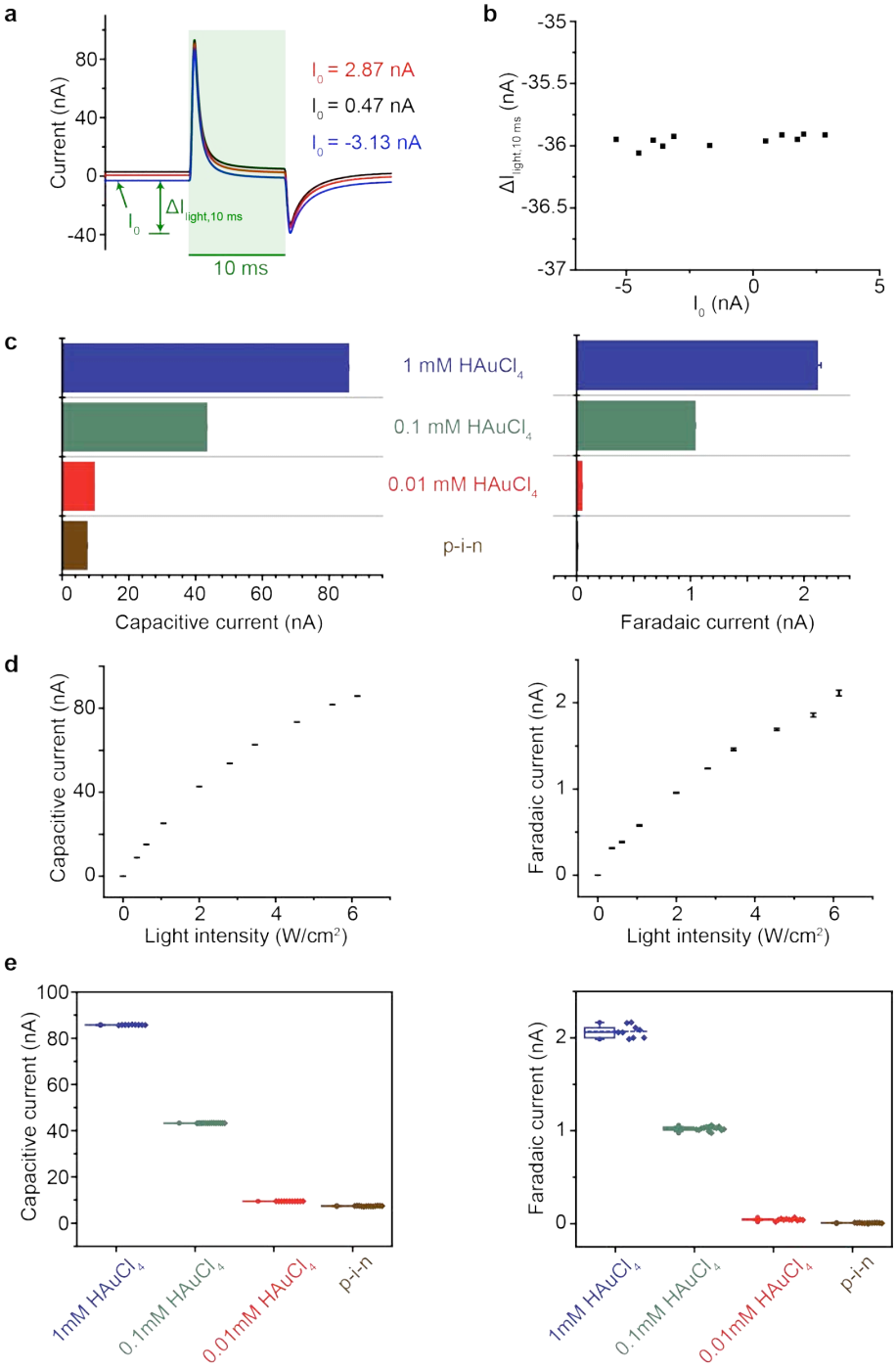

Supplementary Figure 11 | Photo-responses of Au-decorated Si structures. a, Representative current traces recorded from an Au-decorated *p-i-n* membrane (from 1 mM $HAuCl_4$) under LED pulsed illuminations (530 nm, 10 ms, ~ 12.05 mW, ~ 500 μm spot size, ~ 6 W/cm^2) show strong capacitive and Faradaic currents. I_0 is defined as the baseline holding level before the light

illumination. $\Delta I_{\text{light,10 ms}}$ is defined as the maximal relative current amplitude after 10 ms of light illumination with respect to I_0. The light green shaded area marks the light illumination period. **b,** The $\Delta I_{\text{light,10 ms}}$ - I_0 plot shows a negligible slope and a prominent intercept indicating strong photoelectric and weak photothermal responses, similar to that from a pristine *p-i-n* diode junction. **c,** Statistical analyses of capacitive (left) and Faradaic currents (right) from *p-i-n* Si diode junctions with surface Au decorations show that the maximum values of both currents are achieved with Au deposited from 1 mM $HAuCl_4$. Error bars denote standard deviations from the means. Data are from recordings at different holding levels of one representative sample for each Si structure. n=9 for 1 mM $HAuCl_4$, n=14 for 0.1 mM $HAuCl_4$, n=11 for 0.01 mM $HAuCl_4$, n=13 for *p-i-n*. **d,** The amplitudes for both the capacitive (left) and Faradaic currents (right) of an Au-decorated *p-i-n* membrane (prepared from 1 mM $HAuCl_4$) can be monotonically tuned by the light intensity. Error bars denote standard deviations from the means. n=13 for the 0.36 W/cm^2 data point, n=12 for 0.62 W/cm^2, n=12 for 1.06 W/cm^2, n=13 for 2.00 W/cm^2, n=12 for 2.80 W/cm^2, n=10 for 3.46 W/cm^2, n=11 for 4.56 W/cm^2, n=11 for 5.49 W/cm^2, n=9 for 6.14 W/cm^2. **e**, Box-and-whisker plots and raw data points of the capacitive and Faradaic currents as shown in **c**. Half of the data points are within the boxes, 80% are within the whiskers. Solid and dashed lines represent the medians and means, respectively. Round dots mark the maximum and minimum values. Diamond dots represent the raw data points. Data are from recordings at different holding levels of one representative sample for each Si structure. n=9 for 1 mM $HAuCl_4$, n=14 for 0.1 mM $HAuCl_4$, n=11 for 0.01 mM $HAuCl_4$, n=13 for *p-i-n*.

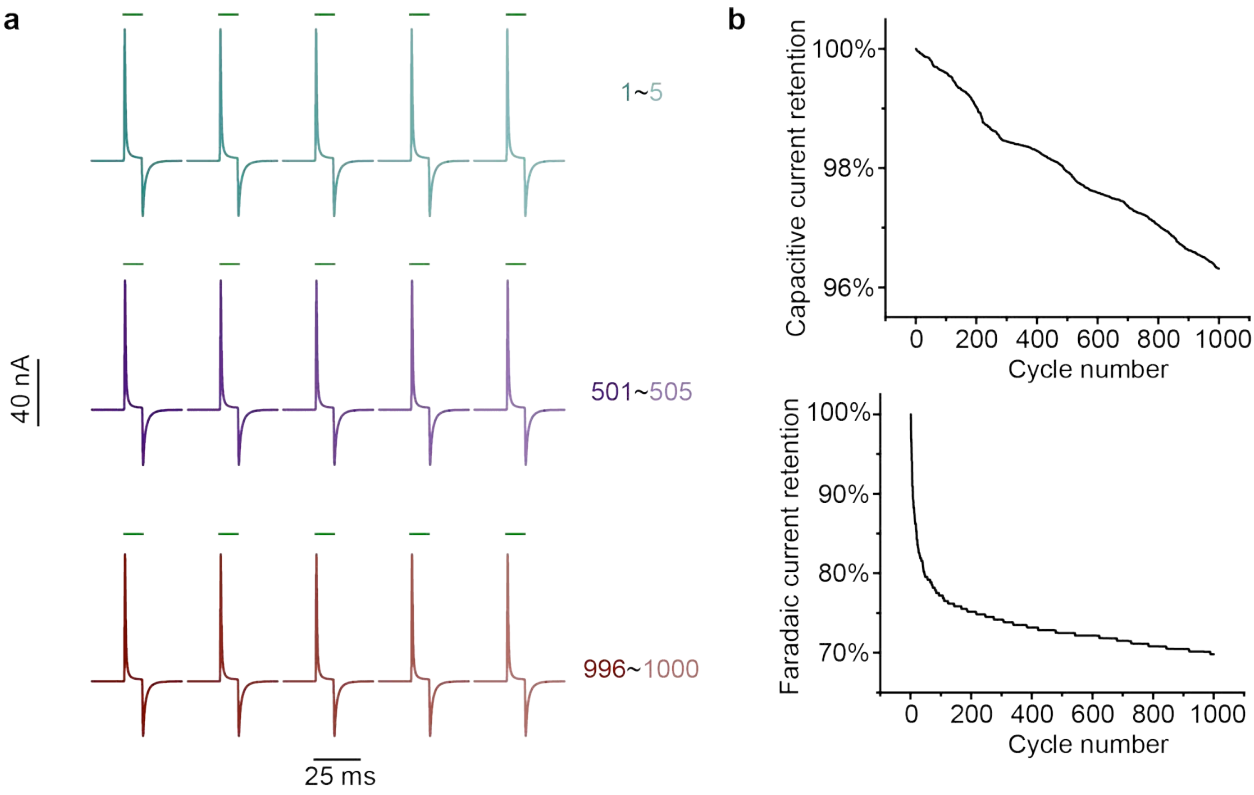

Supplementary Figure 12 | Photoelectric responses of Au-decorated diode junctions possess good stabilities. a, A cyclability test of an Au-decorated *p-i-n* membrane (prepared from 1 mM $HAuCl_4$) with 1000 times of repetitive illuminations (530 nm, 10 ms, ~ 12.05 mW, ~ 500 μm spot size, ~ 6 W/cm^2) at a frequency of 2 Hz. Current traces between cycle number 1 and 5 (green), 501 and 505 (purple), and 996-1000 (brown) are plotted. Green bars denote the 10-ms light illumination periods. **b,** Both the capacitive and Faradaic currents show high retentions after 1000 cycles. Notably, the capacitive current has an even higher cyclability (~ 96% retention) versus the Faradaic current (~ 70% retention), likely benefited from the reversible capacitive charging/discharging processes as oppose to the irreversible surface electrochemical reactions.

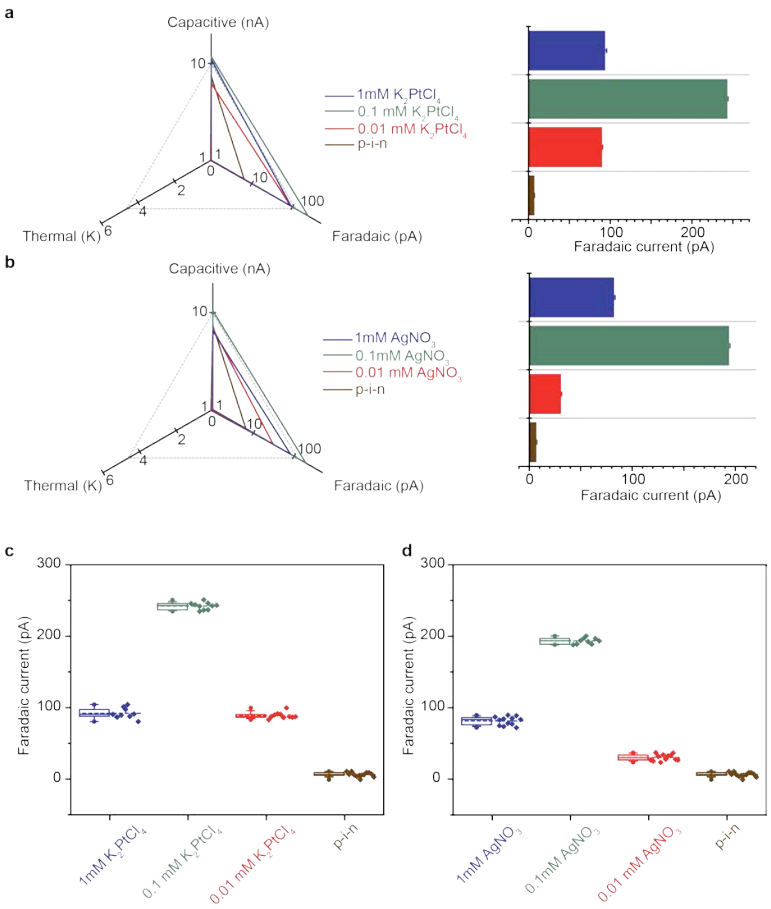

Supplementary Figure 13 | Metal-enabled promotion of photocurrents in *p-i-n* diode junctions are general. Both Pt (**a**) and Ag (**b**) can be deposited to enhance the photoelectric responses of the *p-i-n* diode junction. Maximal Faradaic currents are reached using 0.1 mM of K_2PtCl_4 or $AgNO_3$ although the enhancements enabled by Pt and Ag are not as pronounced comparing to Au. Error bars denote standard deviations from the means. Data are from recordings at different holding levels of one representative sample for each Si structure. **c** and **d**, Box-and-whisker plots and raw data points of the Faradaic currents as shown in **a** and **b**. Half of the data points are within the boxes, 80% are within the whiskers. Solid and dashed lines represent the medians and means, respectively. Round dots mark the maximum and minimum values. Diamond dots represent the raw data points. Data are from recordings at different holding levels of one representative sample for each Si structure. In **a** and **c**, n=9 for 1 mM K_2PtCl_4, n=10 for 0.1 mM K_2PtCl_4, n=10 for 0.01 mM K_2PtCl_4, n=13 for *p-i-n*. In **b** and **d**, n=12 for 1 mM $AgNO_3$, n=9 for 0.1 mM $AgNO_3$, n=12 for 0.01 mM $AgNO_3$, n=13 for *p-i-n*.

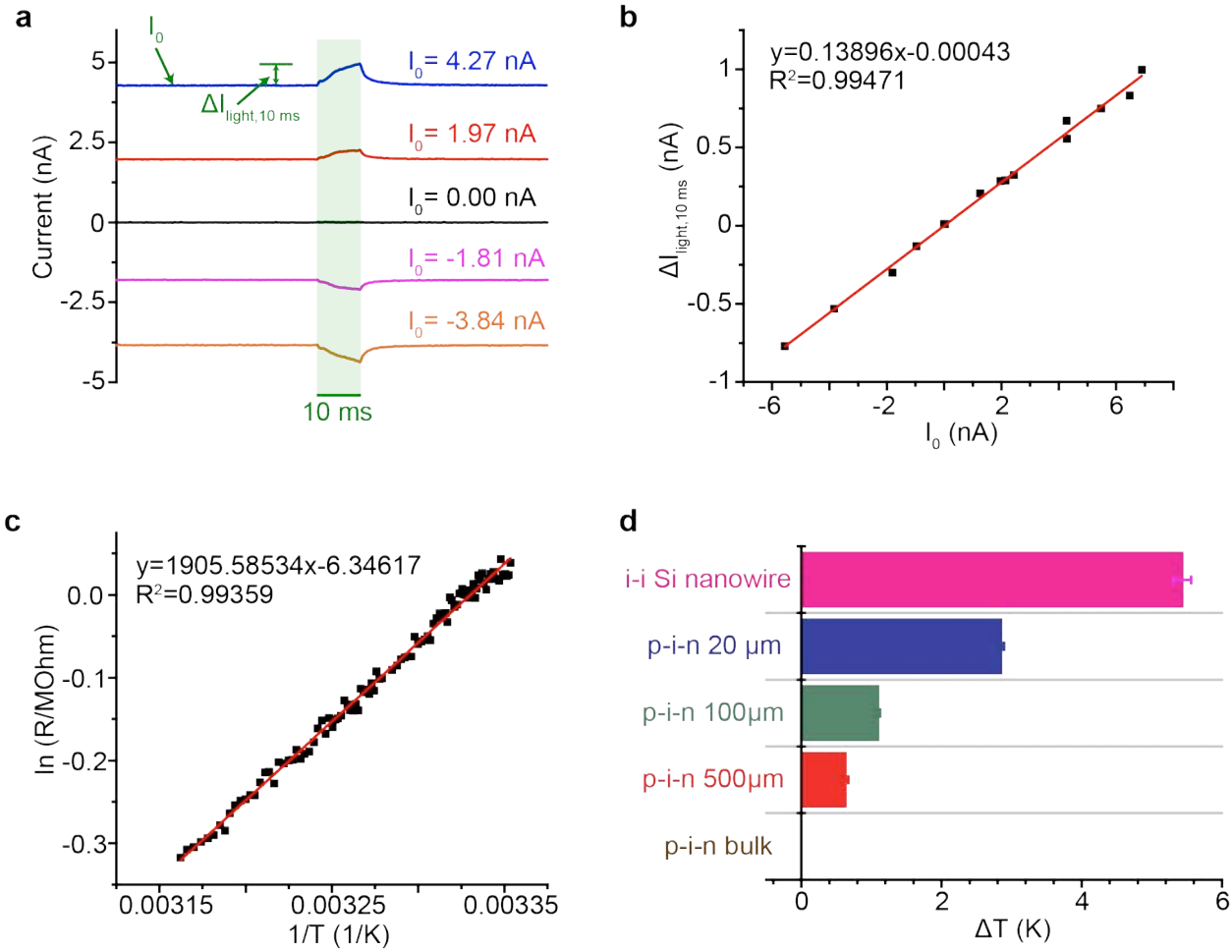

Supplementary Figure 14 | Photo-responses of Si structures with different sizes. a, Representative current traces recorded from an *i-i* nanocrystalline Si nanowire under laser pulses (532 nm, 10 ms, ~ 47.1 mW, ~ 5 μm spot size, ~ 240 kW/cm^2) exhibit a strong dependence on the baseline holding level I_0. $\Delta I_{\text{light,10 ms}}$ is defined as the maximal relative current amplitude after 10 ms of light illumination with respect to I_0. The light green shaded area marks the light illumination period. **b,** The $\Delta I_{\text{light,10 ms}}$ - I_0 plot shows a significant slope and a negligible intercept indicating strong photothermal and weak photoelectric responses. **c,** The pipette resistance over temperature curve calibrated from the same micropipette used for the photo-response measurements. The temperature increase of the PBS solution caused by the photothermal effect are calculated using both the $\Delta I_{\text{light,10 ms}}$ - I_0 plot and the *T-R* calibration curve. Briefly, the resistance of the pipette will decrease after 10 ms of illumination on the Si material due to the photothermal heating of the local PBS solution. The current amplitude during the light

illumination will change accordingly following the Ohm's law. The relationship between the pipette resistances after 0 ms (R_0) and 10 ms ($R_{10\ ms}$) of illumination can then be linked by $R_{10\ ms}=R_0/(1+k)$, where k is the fitted slope value of the $\Delta I_{light,10\ ms}$ - I_0. The temperature increase of the solution can then be inferred using the *T*-*R* calibration curve. **d,** Statistical analyses of the thermal responses of Si structures with different sizes show that the photothermal effect becomes more pronounced with the reduction of Si dimension. *p*-*i*-*n* diode junctions with different sizes were created by a combination of e-beam lithography and reactive ion etching processes. The temperature increase was calculated by the fitted slope of the $\Delta I_{light,10\ ms}$ - I_0, see **Methods** for details. Error bars are the fitting errors from the fitted values. Data are from recordings at different holding levels of one representative sample for each Si structure. n=20 for *i*-*i* Si nanowire, n=12 for *p*-*i*-*n* diode junctions with 20-μm diameters, n=16 for *p*-*i*-*n* diode junctions with 100-μm diameters, n=12 for *p*-*i*-*n* diode junctions with 500-μm diameters, n=14 for bulk *p*-*i*-*n* diode junctions.

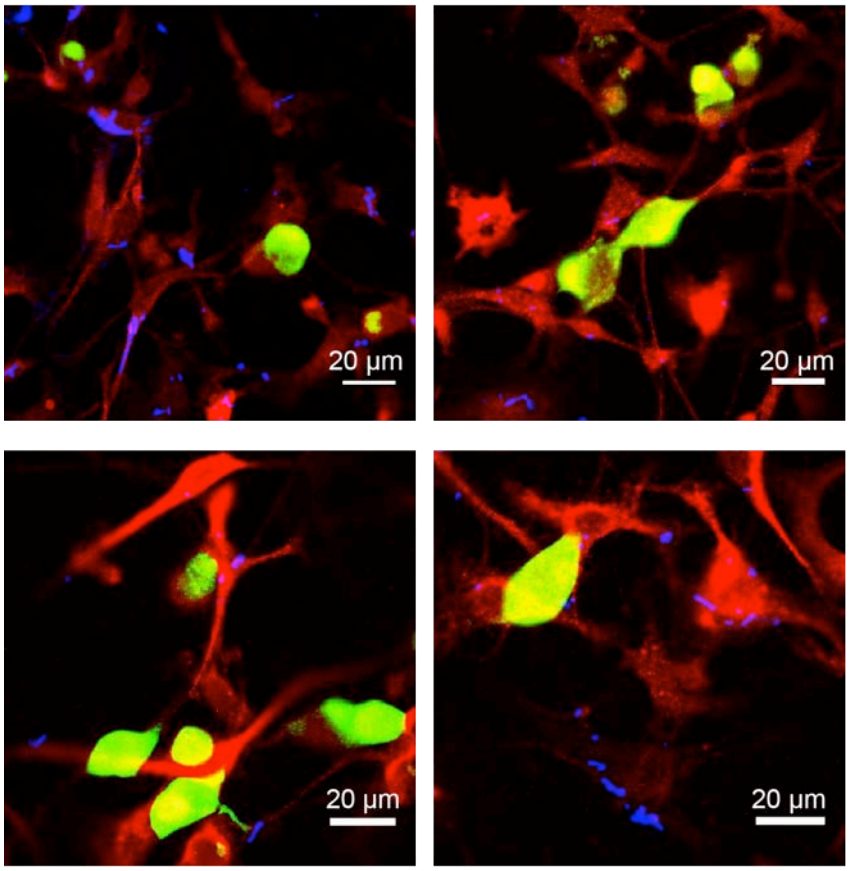

Supplementary Figure 15 | Nanocrystalline Si nanowires display cell-type specific overlapping with glial cells. Overlaid confocal microscope images of the DRG-glia system show that nanowires (blue, scattered light signal) mostly overlap with glial cells (red, GFAP) versus neurons (green, NeuN). The fact that the overlapping nanowires exhibit alignment with cellular protrusions and perinucleus clustering rather than random intracellular distributions suggests that nanowires are internalized by the glial cells.

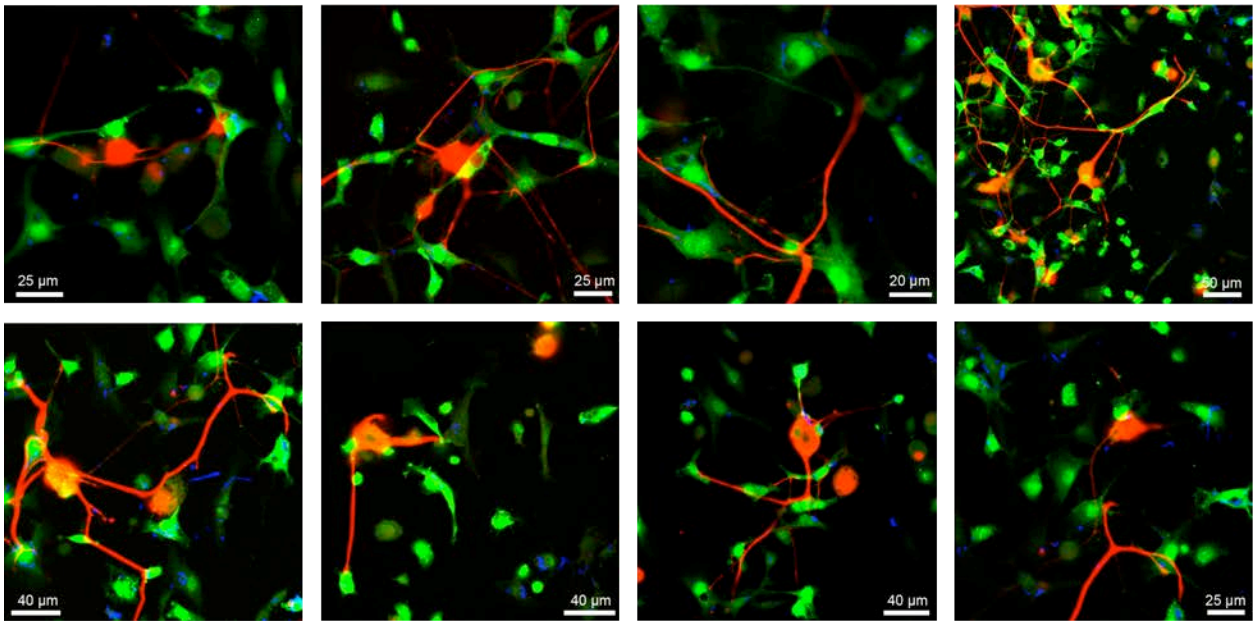

Supplementary Figure 16 | Nanocrystalline Si nanowires display cell-type specific overlapping with glial cells. Overlaid confocal microscope images of the DRG-glia system stained with another set of biomarkers confirm that nanowires (blue, scattered light signal) mostly overlap with glial cells (green, S-100) versus neurons (red, Neurofilament). The existence of the naturally occurring neural-glial junctions suggests the potential of realizing remote neuromodulation with glial cell internalized nanowires.

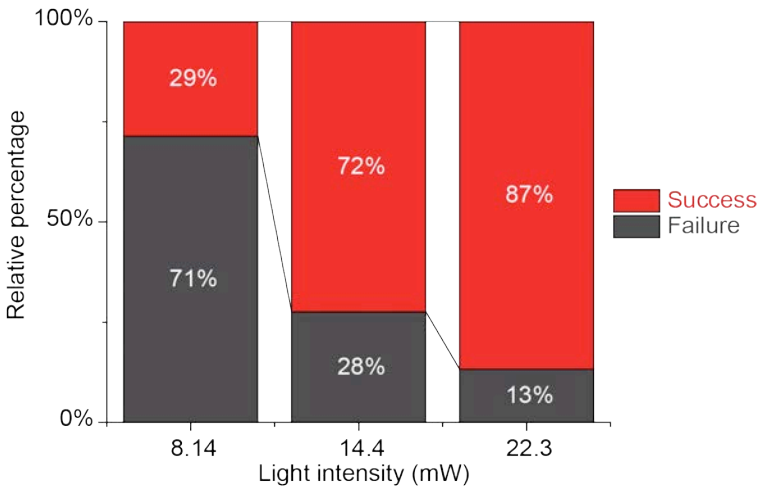

Supplementary Figure 17 | The success rate of intracellular calcium modulation of glial cells is light intensity dependent. The stacked column plot presents the relative success/failure rates of the light-controlled calcium modulation experiment using glial cell internalized nanowires (592 nm, 1 ms, ~ 237 nm spot size). The success rate of eliciting calcium flux increases progressively with higher light intensities. Statistics are from 14 cells for the 8.14-mW light intensity, 76 cells for the 14.4-mW one, and 15 cells for 22.3-mW one.

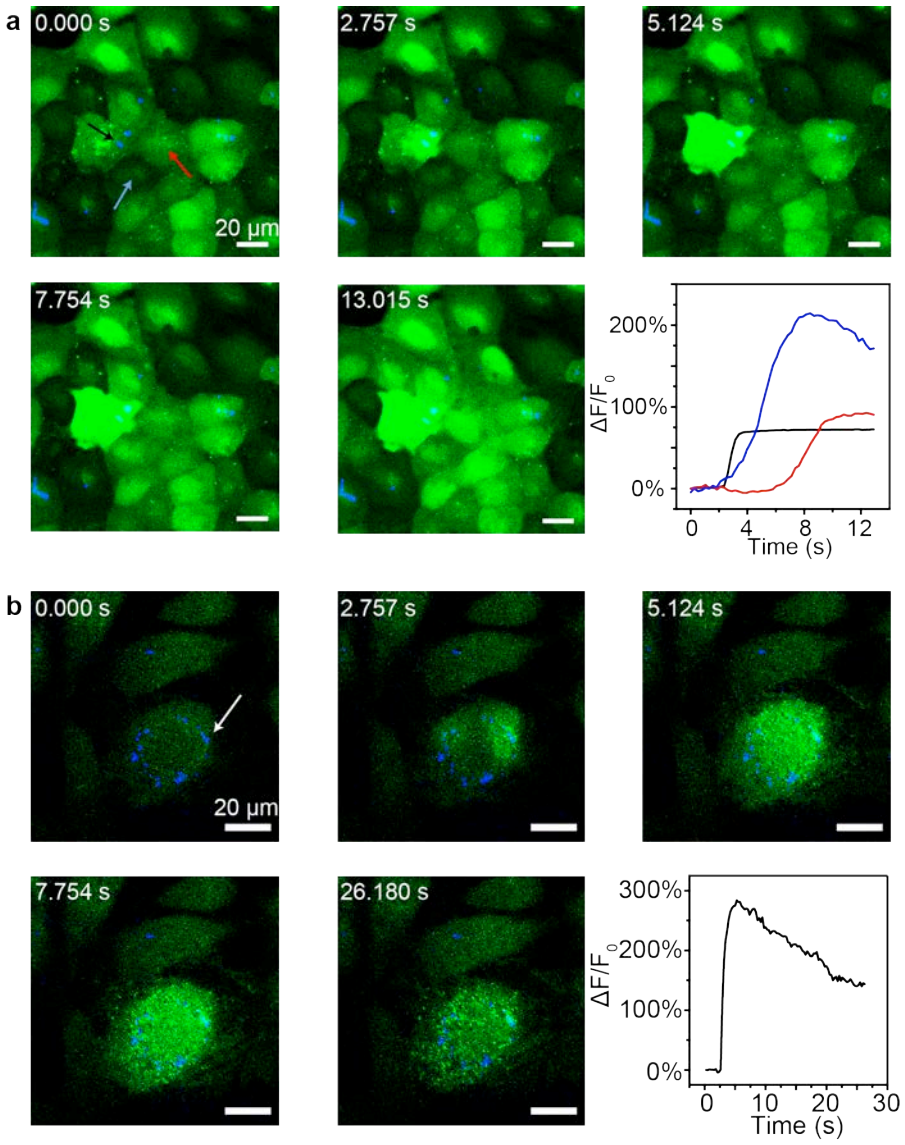

Supplementary Figure 18 | Intracellular stimulation can be extended to multiple cell lines. A cancer cell line, U2OS (**a**), and an endothelial cell line, HUVEC (**b**), can both be stimulated intracellularly to elicit the calcium dynamics. Since the intracellular stimulation of calcium largely utilizes the internal calcium storage organelles rather than ion channels on the plasma membranes, this modulation method is general to a broad range of mammalian cells. The stimulation laser (592 nm, ~ 14.4 mW, ~ 237 nm spot size) was on for 1 ms right before the time point of 2.757 s. Green, calcium; blue, Si nanowires (scattered light). The black arrow marks the nanowire under stimulation, the blue and red arrows mark two adjacent cells of interest in **a**. The white arrow marks the nanowire under stimulation in **b**.

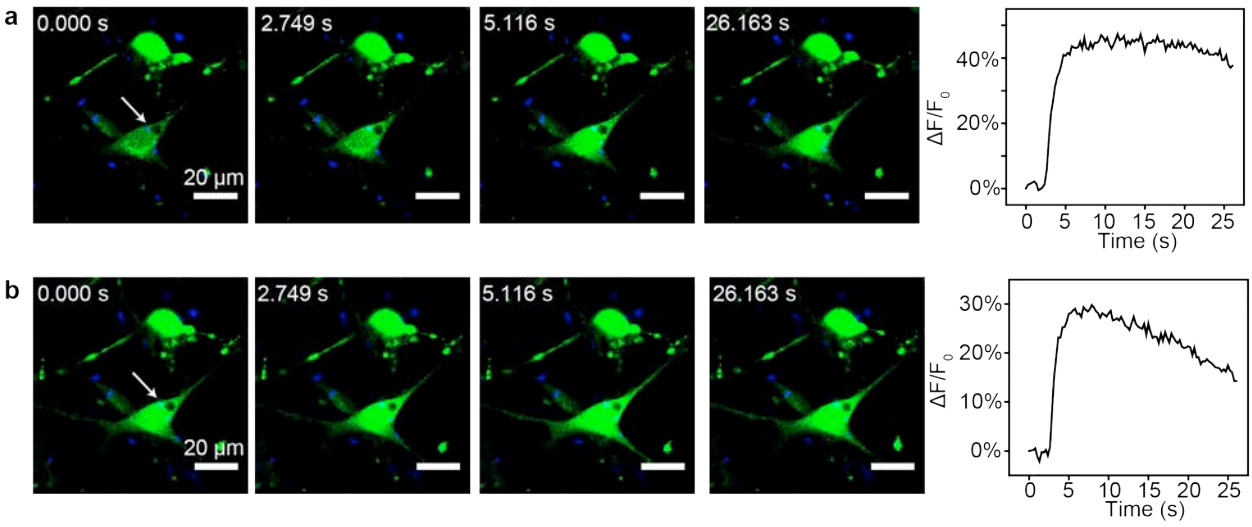

Supplementary Figure 19 | Calcium imaging shows that Si-enabled intracellular stimulation can be performed for multiple times. a and **b,** The same glial cell with internalized Si nanowires (green, calcium; blue, Si nanowires) was stimulated repetitively without being killed. In the second time of stimulation (**b**), the intracellular calcium concentration can still increase even it is not at its base level. The stimulation laser (592 nm, ~ 14.4 mW, ~ 237 nm spot size) was on for 1 ms right before the time point of 2.749 s. White arrows mark the same nanowire under stimulation.

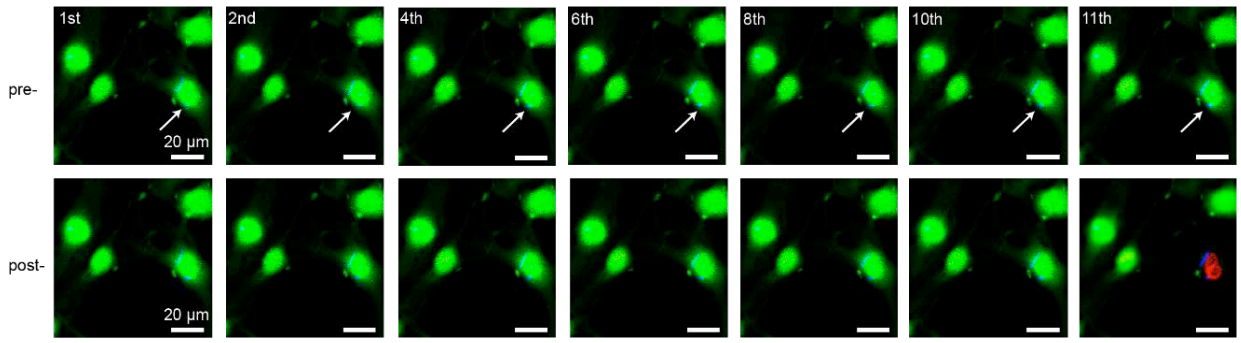

Supplementary Figure 20 | LIVE/DEAD assay shows that intracellular photostimulation is minimally invasive. The same glial cell with internalized Si nanowires (green, calcein; blue, Si nanowires) was stimulated intracellularly for ten consecutive times without being killed. The stimulation condition was ~ 32.2 mW for 1 ms (~ twice of the laser power used for calcium elevation) in the first ten cycles using a 592 nm laser (~ 237 nm spot size). The cell was killed (red, ethidium homodimer-1; blue, Si nanowires) after a 1-ms pulse of ~ 54.1 mW laser (~ four times of the laser power used for calcium elevation, 592 nm, ~ 237 nm spot size) was delivered. White arrows mark the laser stimulation sites.

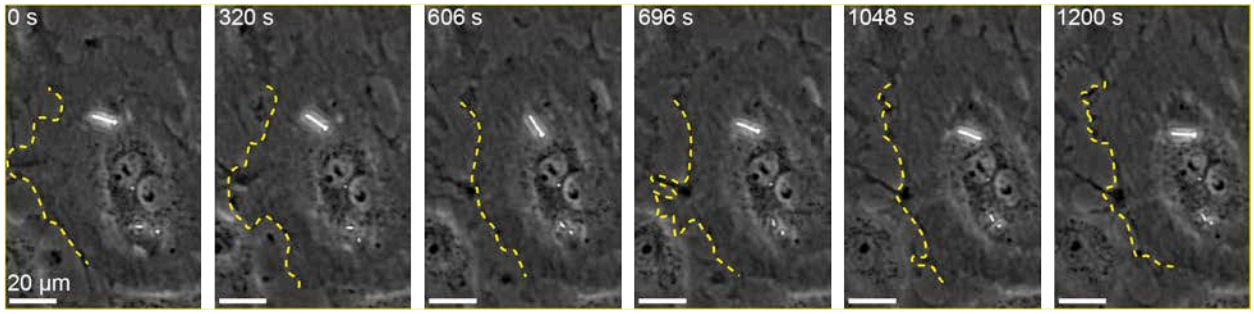

Supplementary Figure 21 | Intracellular Si-based biointerfaces represent a motile system for cellular modulation. Time-lapse phase-contrast image series of a HUVEC cell with internalized nanowires. The cell itself dynamically changed its morphology (marked by dashed yellow lines) and moved constantly over time while the relative orientation and location of the internalized nanowire also underwent rapid movements. This motile biointerface may be further developed to target various intracellular compartments at different stages of the internalization process or modulate surrounding cells at different locations over time.

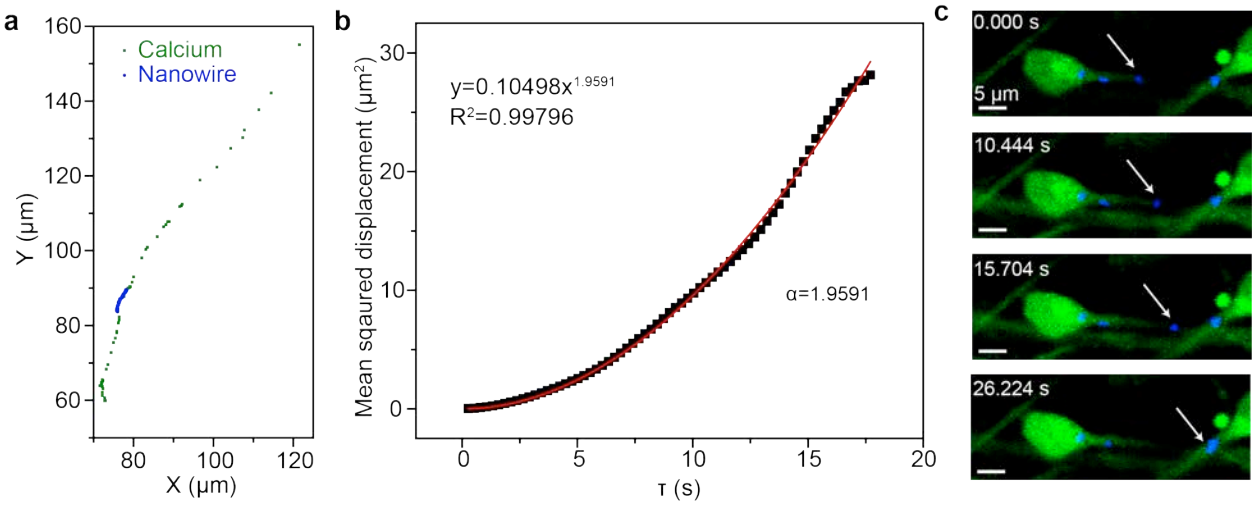

Supplementary Figure 22 | Calcium wave propagation and nanowire transport were correlated. a, Trajectories of the nanowire movement and the calcium wave-front propagation are overlaid, indicating that the nanowire was transported inside the cell protrusion. **b,** Mean-squared displacement analysis of the nanowire motion recorded after the calcium wave-front reached its original location, showing a diffusivity coefficient $\alpha \sim 2$ and suggesting that a temporary active transport motion of the nanowire could be triggered by intracellular calcium concentration elevation. The exact mechanism is unknown. **c,** An additional image series (green, calcium; blue, Si nanowires) from a different example, showing a similar calcium-triggered unidirectional nanowire transport. White arrows indicate the nanowire of interest serving as a transport marker.

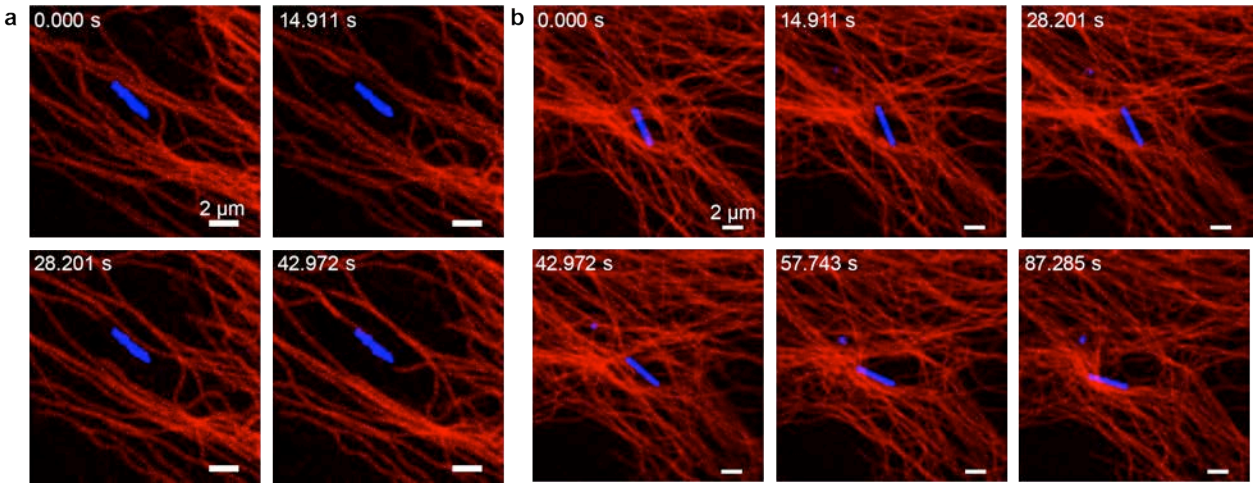

Supplementary Figure 23 | Microtubule networks can be remotely manipulated by intracellular stimulation of Si nanowires. a and **b**, Two live cell imaging series (red, microtubules; blue, Si nanowires) showing deformation of microtubule networks by the laser illuminations (592 nm, ~ 2.09 mW, ~ 211 nm spot size) of internalized Si nanowires. The laser pulses were 1 ms long before the time point of 14.911 s. The cells were alive after the remote cytoskeletal manipulation.

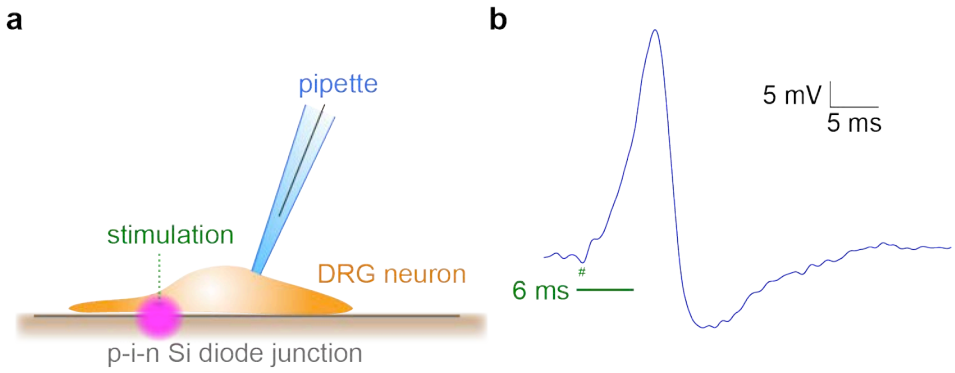

Supplementary Figure 24 | DRG neurons cultured on a *p-i-n* Si diode junction can be optically stimulated. a, A schematic illustration of photostimulation of DRG neurons cultured on a Si diode junction substrate. **b,** A 6 ms-long laser pulse (532 nm, ~ 47.1 mW, ~ 5 μm spot size) can elicit an action potential of the patched neuron. # marks the photoelectric artifact coinciding with the light onset[58,59]. The photothermal effect is minimal in this device configuration.

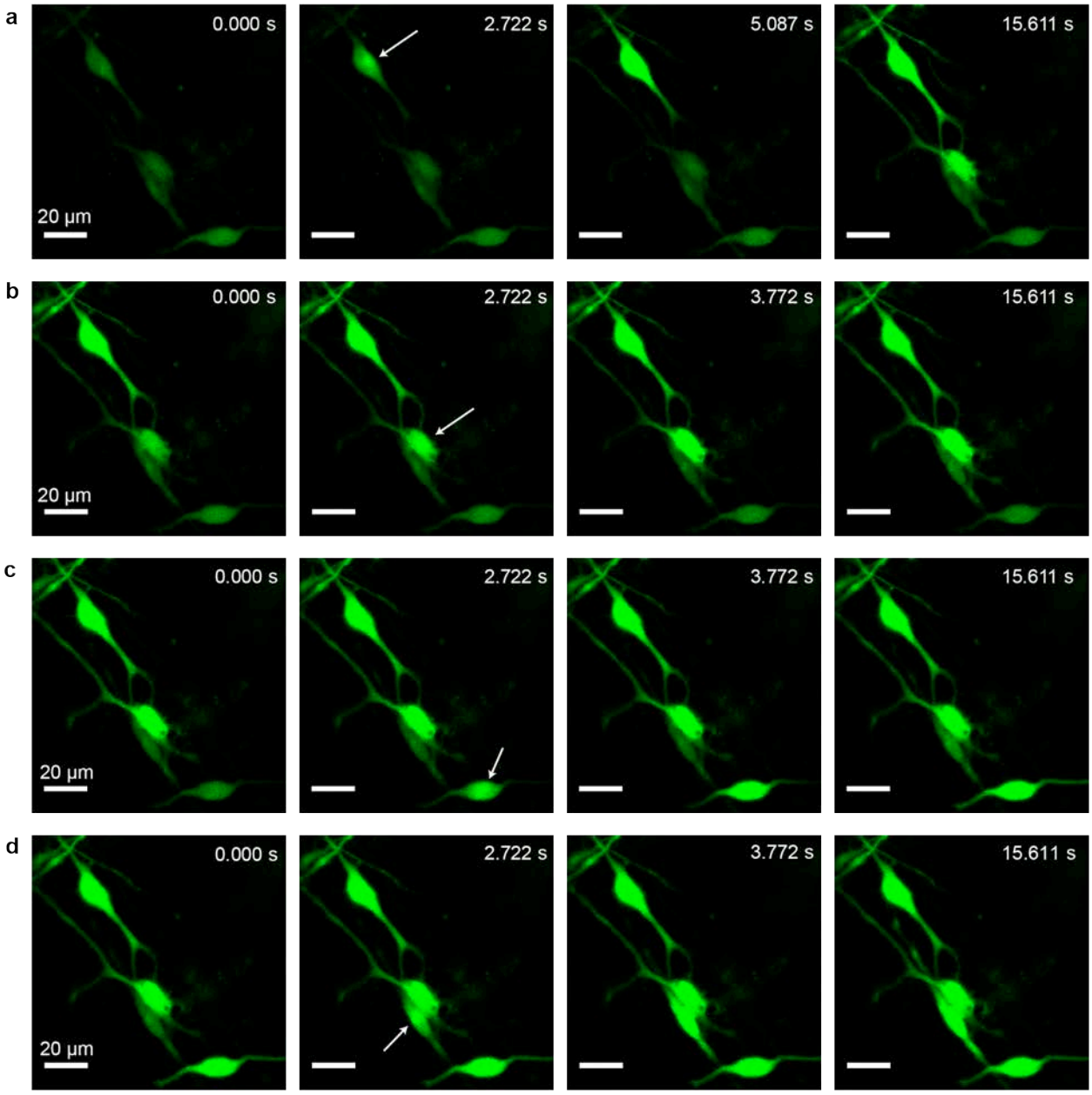

Supplementary Figure 25 | *p-i-n* Si diode junctions enable high spatiotemporal-resolution extracellular stimulations of calcium dynamics. a-d, Laser illuminations (592 nm, ~ 14.4 mW) of different cells in a DRG culture (green: calcium) on a *p-i-n* Si diode junction, showing stepwise cellular modulation. The illuminations induce localized and fast calcium elevations near the stimulation sites and subsequent calcium wave propagations both intra- and inter-cellularly. Laser stimulations were 1 ms long before the time point of 2.722 s. White arrows mark the laser stimulation sites.

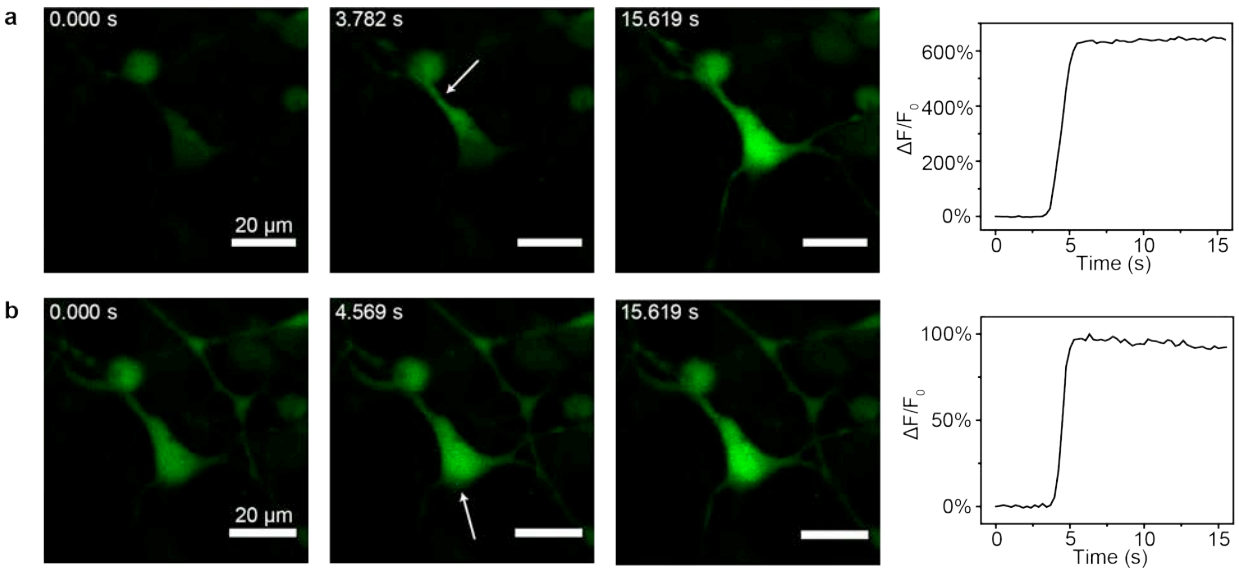

Supplementary Figure 26 | Calcium imaging shows that Si-enabled extracellular stimulation can be performed for multiple times. a and **b,** The same glial cell cultured on a *p-i-n* Si diode junction (green, calcium) is stimulated extracellularly in two consecutive series without being damaged. As shown in the first time of stimulation (**a**), not only the cell body but also the protrusion can be stimulated to induce the cellular calcium dynamics. The stimulation laser (592 nm, ~ 14.4 mW) was on for 1 ms right before the time point of 3.782 s in each case. White arrows mark the laser stimulation sites.

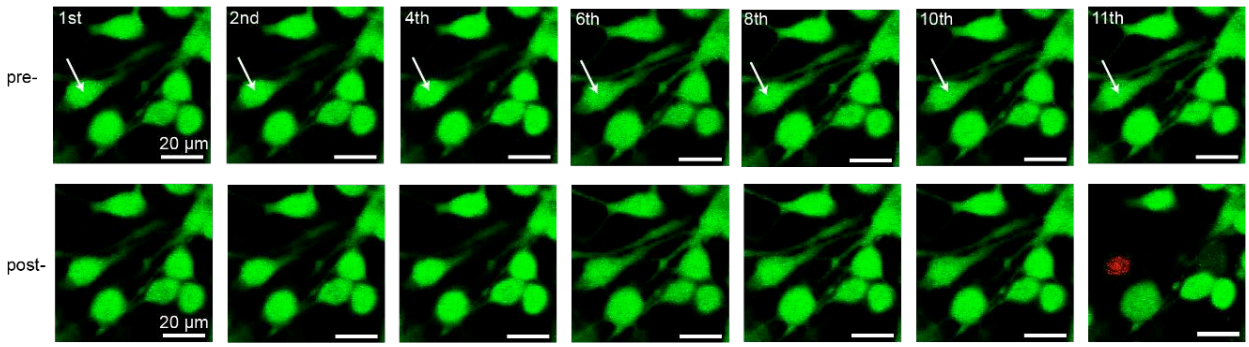

Supplementary Figure 27 | LIVE/DEAD assay shows that extracellular photostimulation is minimally invasive. The same glial cell cultured on a *p-i-n* Si junction (green, calcein) was stimulated extracellularly for ten consecutive times without being killed. The stimulation condition was ~ 54.1 mW for 1 ms (~ four times of the laser power needed for calcium elevation) in the first ten cycles using a 592 nm laser (~ six times of the laser power needed for calcium elevation). The cell was killed (red, ethidium homodimer-1) after a 1-ms pulse of ~ 79.5 mW laser was delivered. White arrows mark the laser stimulation sites.

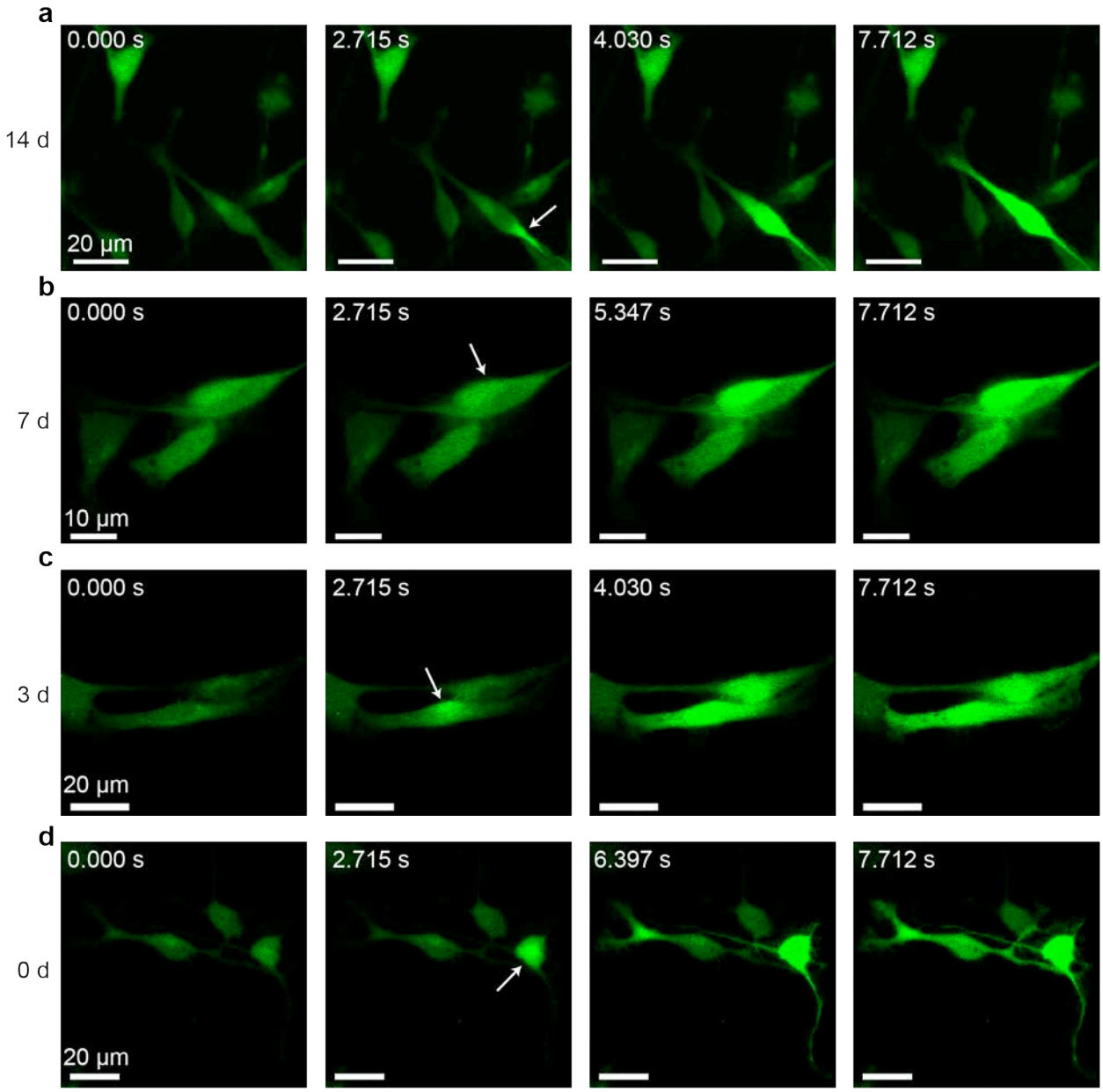

Supplementary Figure 28 | Extracellular photostimulation of calcium dynamics can be performed over solution-degraded Si surfaces. Si *p-i-n* membranes were immersed in PBS solutions under 37 ^{o}C for various durations (**a**, 14 days; **b**, 7 days; **c**, 3 days; **d**, 0 day) prior to the culture and subsequent photostimulations. The threshold intensity (**a**, 42.7 mW; **b**, 32.2 mW; **c**, 22.3 mW; **d**, 14.4 mW) of the laser (592 nm) to elicit calcium dynamics gradually increases for cells cultured on substrates with a longer immersion period. The laser was on for 1 ms right before the time point 2.715 s. White arrows mark the laser stimulation sites.

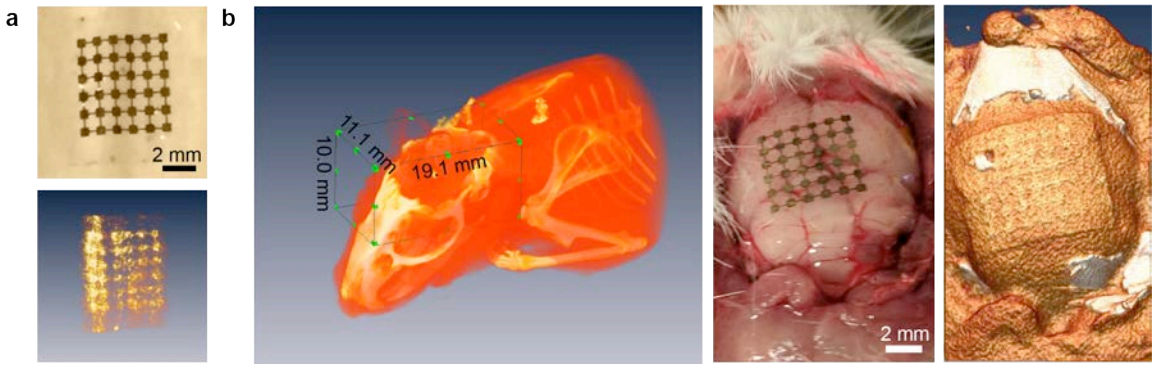

Supplementary Figure 29 | Distributed Si mesh form conformal interfaces with the brain cortex. a, A photograph (upper) and its corresponding micro computed tomography (CT) image (lower) of a flexible device made of a Si mesh a PDMS layer. The surface decoration with Au also provides additional contrast under x-ray scans. **b,** The device can conformally coat the mouse brain cortex as shown both by the photograph (middle) and the CT image (right).

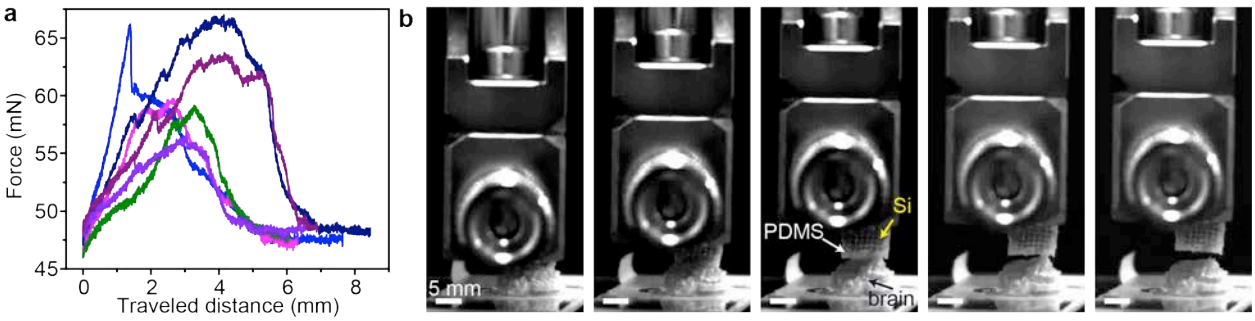

Supplementary Figure 30 | The flexible device made of Si and PDMS is adhesive to the brain tissue. a, Representative force-extension curves recorded during the peelings of the device from the brain cortex yielding an average adhesion energy of 1.34 ± 0.63 J/m^2 (mean ± standard deviation) from 6 trials of measurements. **b,** Snapshots of a typical peeling test showing the adhesion between the device and the brain when detaching.

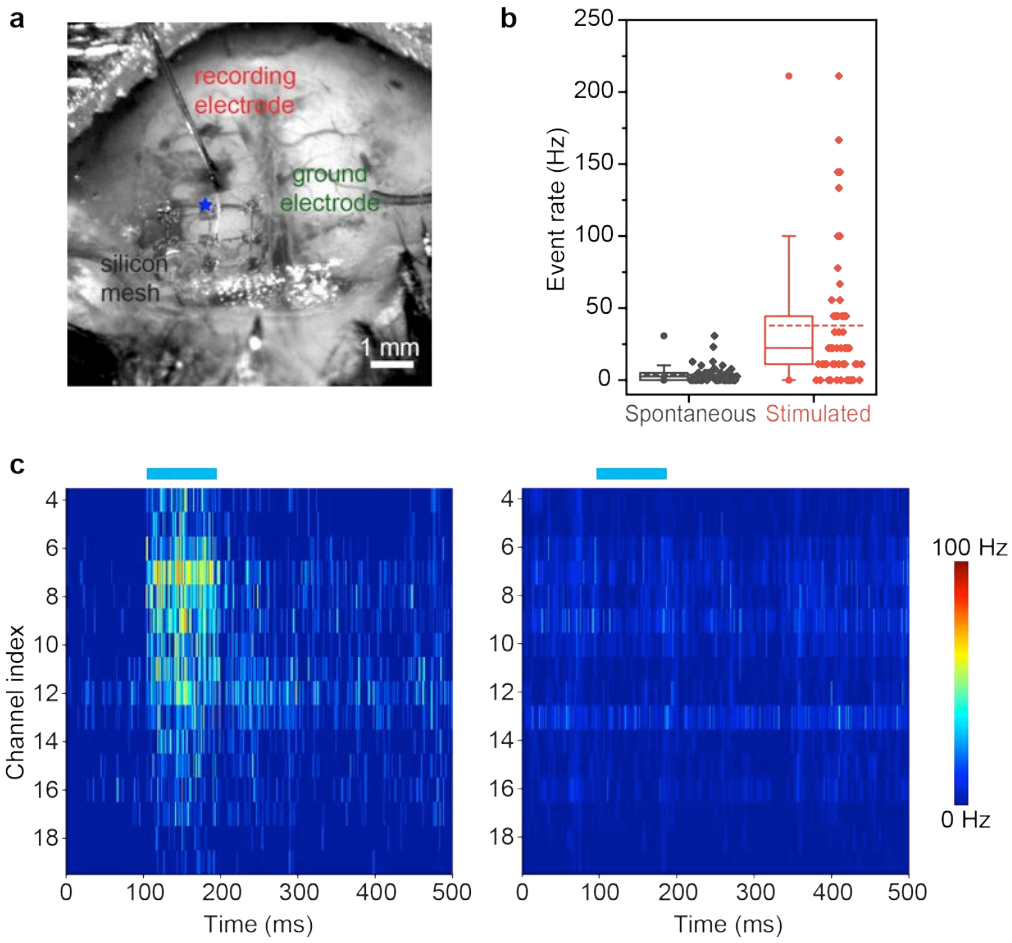

Supplementary Figure 31 | The recorded brain responses under illumination is due to the Si mesh. a, The experimental paradigm of an *in vivo* photostimulation test. A linear probe is inserted into the somatosensory cortex with an attached Si mesh in the close proximity. The laser illumination site (473 nm, ~ 216 μm spot size) is marked by a blue star. **b,** The mean evoked response rate (~ 37.9 Hz) is significantly different from the spontaneous one (~ 3.7 Hz). Half of the data points are within the boxes, 80% are within the whiskers. Solid and dashed lines represent the medians and means, respectively. Round dots mark the maximum and minimum values. Diamond dots represent the raw data points. Two-sided paired *t*-test, $p=4\times10^{-6}$. Event rates were calculated from channel 9 with the 5-mW and 100-ms stimulation condition (n=50 trials from a representative photostimulation experiment on one mouse). **c,** Recordings from a control experiment without the Si mesh (right) did not yield significant signal differences under illumination. Cyan bars mark the illumination periods.

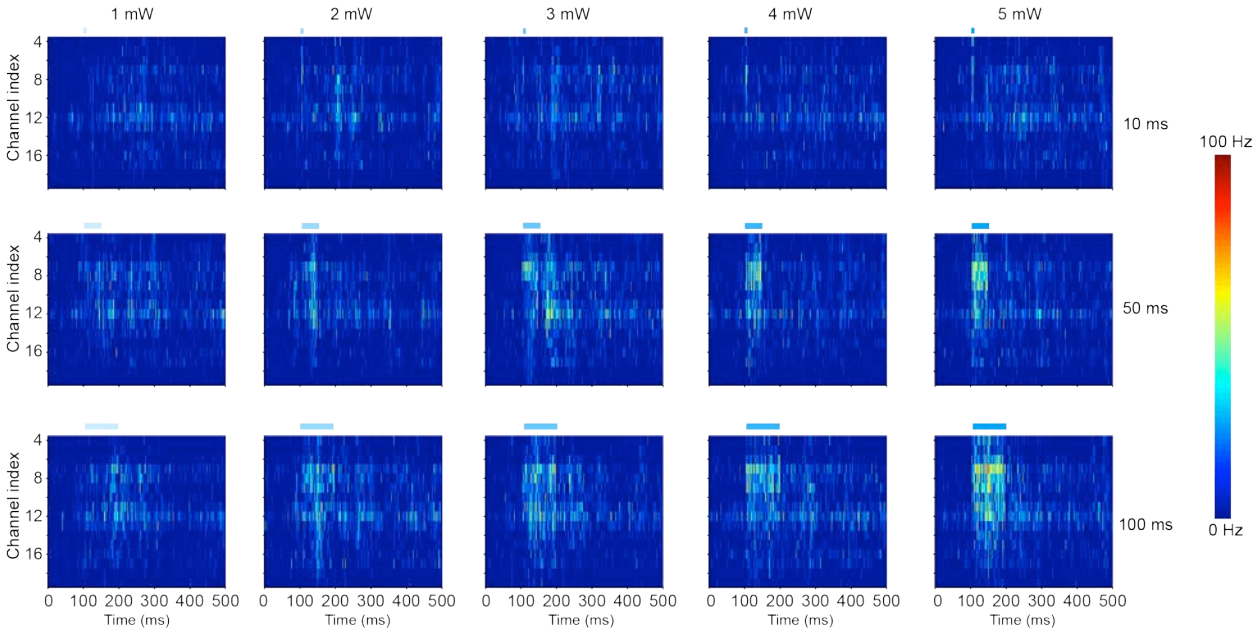

Supplementary Figure 32 | The stimulated neural response is controllable. Parametric stimulations with varied laser powers and durations (1~5 mW, 10 ms, 50 ms, 100 ms) show a positive correlation between the evoked event rate and the stimulation power, which is essential to the predictive control of the Si mesh as a precise neuromodulator. Cyan bars with different transparencies indicate illumination periods with different laser powers.

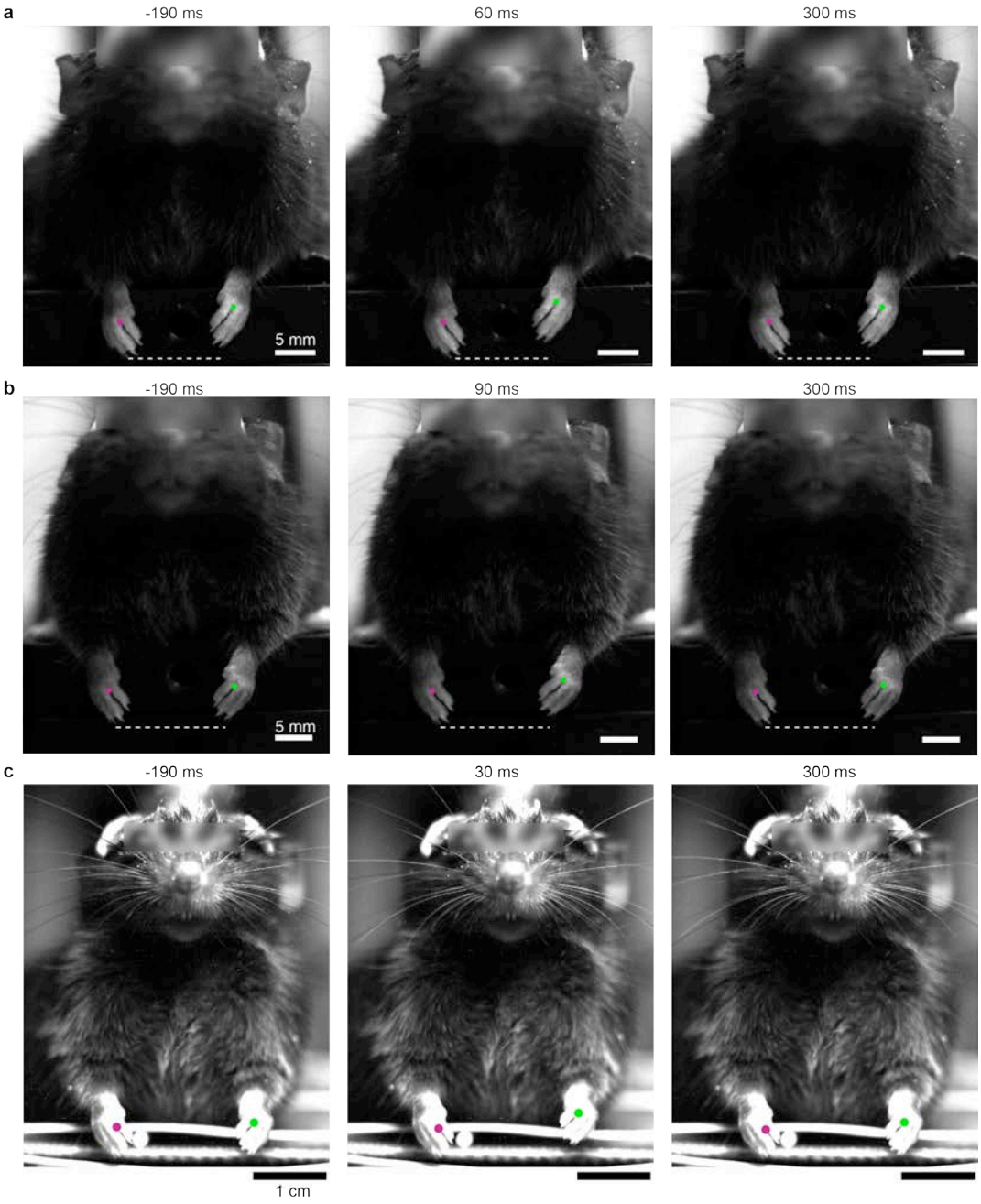

Supplementary Figure 33 | Photostimulation of the Si mesh can trigger mouse forelimb movements. More examples showing the preferred left forelimb movements following the laser illuminations (50 ms, ~ 5 mW for **a**; 100 ms, ~ 4 mW for **b**; 50 ms, ~ 4 mW for **c**, 473 nm, ~ 216 μm spot size) of Si meshes attached to the right side of the forelimb primary motor cortex. See **Supplementary Video 2** for more details. The 0 ms time point denotes the light onset. White dashed lines in **a** and **b** were drawn to highlight the longitudinal movements of the left forelimbs.

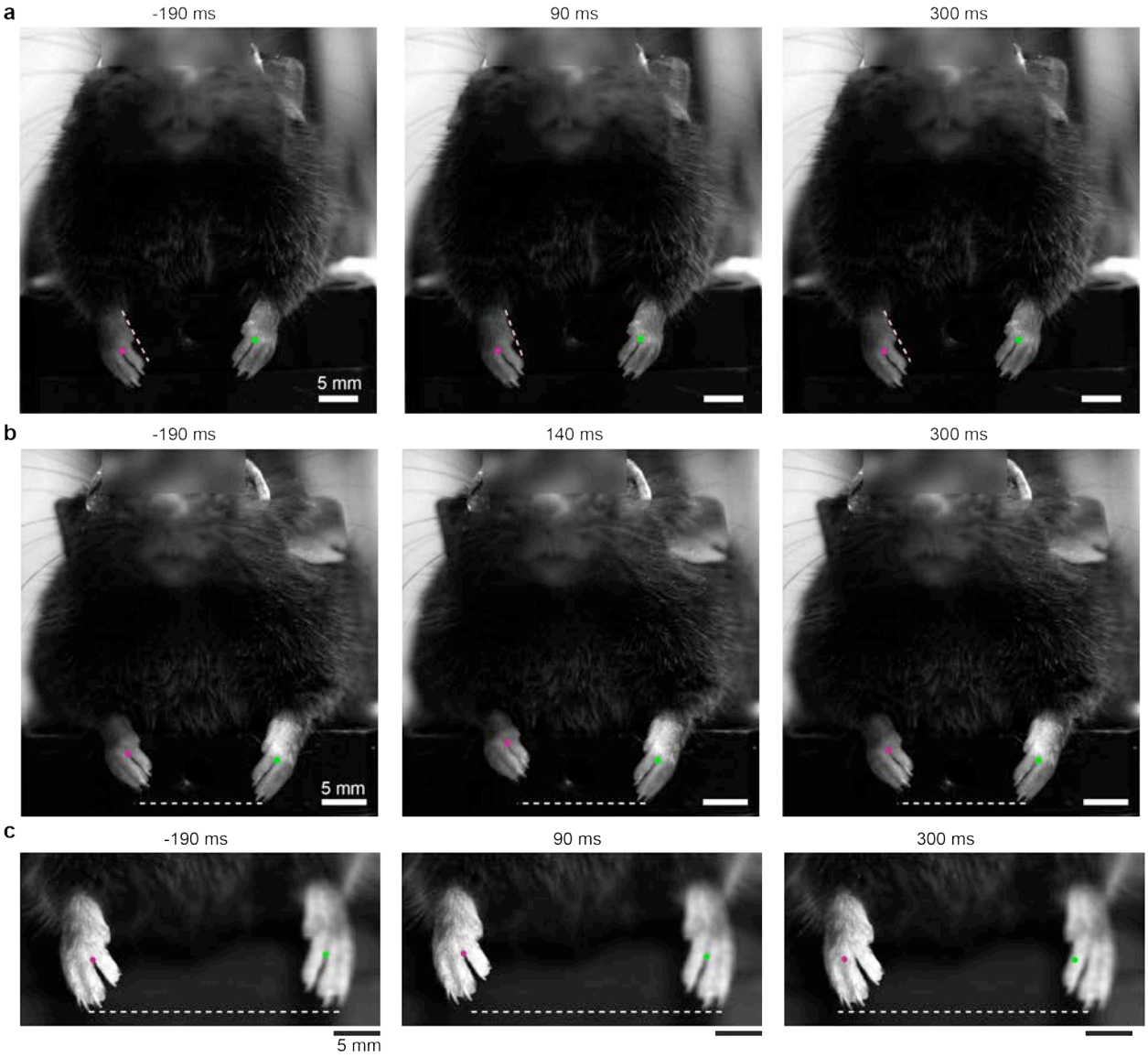

Supplementary Figure 34 | Photostimulation of the forelimb motor cortex triggers the contra side forelimb preferred movement. The right forelimb movements can be triggered by the laser illuminations (50 ms, ~ 1 mW for **a**; 50 ms, ~ 5 mW for **b**; 100 ms, ~ 5 mW for **c**, 473 nm, ~ 216 μm spot size) of Si meshes attached to the left side of the forelimb primary motor cortex. See **Supplementary Videos 3** and **4** for more details. The 0 ms time point denotes the light onset. The right forelimb in **a** underwent a lateral movements after the stimulation as indicated by the changes of the pink dashed line orientations. White dashed lines in **b** and **c** were drawn to highlight the longitudinal movements of the right forelimbs.

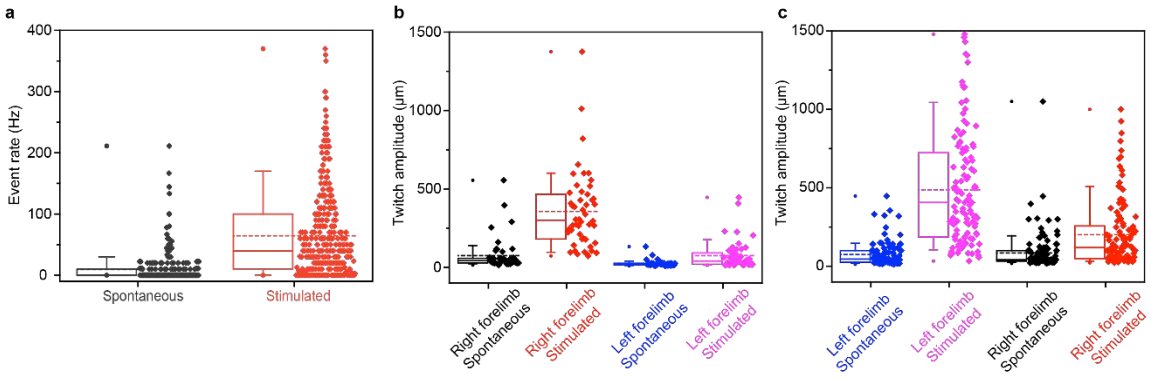

Supplementary Figure 35 | Quantitative comparisons of brain activities and forelimb movements before and after photostimulations. a, The mean spontaneous response rate (~ 9.4 Hz) is significantly smaller from the evoked one (~ 64.3 Hz). Two-sided paired *t*-test, $p=3.8\times10^{-34}$. Event rates were calculated from the 5-mW and 100-ms stimulation condition. $n=371$ trials from photostimulation experiments on three different mice. **b** and **c**, Photostimulations of Si meshes attached to the primary motor cortex (**b**, left cortex; **c**, right cortex) evoked movements of contralateral forelimbs (**b**, right forelimb; **c**, left forelimb) with significantly higher twitch amplitudes than the ipsilateral ones (**b**, left forelimb; **c**, right forelimb). Two-sided paired *t*-test of contralateral versus ipsilateral movements after stimulations, $p=9.9\times10^{-11}$ in **b**, $p=1.0\times10^{-22}$ in **c**. Two-sided paired *t*-test of stimulated versus spontaneous contralateral movements, $p=9.6\times10^{-15}$ in **b**, $p=9.5\times10^{-26}$ in **c**. $n=50$ trials from photostimulation experiments on four mice in **b**, $n=119$ trials from photostimulation experiments on five mice in **c**. Half of the data points are within the boxes, 80% are within the whiskers. Solid and dashed lines represent the medians and means, respectively. Round dots mark the maximum and minimum values. Diamond dots represent the raw data points.

Material	Bandgap (eV)	Biocompatibility	Biodegradability	Form	Cost
Silicon (Si)	1.1, indirect	Good	Degradable in biological fluids	Bulk wafers, membranes, nanowires	Low
Gold (Au)	N/A	Good	Non-degradable	Nanowires, nanoparticles	High
Platinum (Pt)	N/A	Good	Non-degradable	Nanowires, nanoparticles	High
Carbon (C)	N/A	Good	Non-degradable	Graphene, carbon nanotubes, diamond	Low
Indium phosphide (InP)	1.35, direct	Moderate	Non-degradable	Bulk wafers, nanowires, nanoparticles	High
Indium arsenide (InAs)	0.36, direct	Moderate	Non-degradable	Bulk wafers, nanowires, nanoparticles	High
Gallium Phosphide (GaP)	2.26, indirect	Moderate	Non-degradable	Bulk wafers, nanowires, nanoparticles	High
Gallium Arsenide (GaAs)	1.43, direct	Moderate	Non-degradable	Bulk wafers, Nanowires, nanoparticles	High
Titanium oxide (TiO_2)	3.2, indirect (anatase); 3.02, direct (rutile)	Moderate	Non-degradable	Nanowires, nanoparticles	Low
Zinc oxide (ZnO)	3.37, direct	Moderate	Non-degradable	Nanowires, nanoparticles	Low
Indium Tin Oxide (ITO)	~4, direct	Good	Non-degradable	Thin film	Moderate
Cadmium sulfide (CdS)	2.42, direct	Toxic	Non-degradable	Nanowires, nanoparticles	Moderate
Cadmium Selenide (CdSe)	1.74, direct	Toxic	Non-degradable	Nanowires, nanoparticles	Moderate

Supplementary Table 1 | Comparison of multiple material candidates for light-controlled multi-scale biointerfaces. First of all, as a semiconductor, Si can induce both the photothermal and photoelectric (including capacitive and Faradaic) processes, whereas metals such as Au display primarily the photothermal effect when plasmonic heating becomes effective (which limits its potential applications for certain biophysical and biomedical studies). Similarly, although carbon and Pt-based materials have been the major systems in electrochemical and related biomedical research, they typically do not display prominent or controllable photoelectric

properties which makes them challenging for the photoelectric biointerfaces shown in this work. Secondly, both the industrial and synthetic processes for Si are well established, which enables the facile fabrication of various Si forms across multiple length scales. For other semiconductors, such as InP and GaP, although they can also exist in forms similar to Si, their fabrication processes typically require higher costs and more sophisticated instrumentation. Additionally, for light-controlled semiconductor-based biointerfaces, the material bandgap is critical as it determines the wavelength range at which the device can be operated. Unlike Si, which absorbs light up to the NIR region, other common semiconductors, *e.g.,* TiO_2, GaP, ZnO, and CdS, have larger bandgaps and therefore can only work in the ultraviolet-blue region. Finally, Si is not only biocompatible but also biodegradable, which may be important for the future implementation of transient biointerfaces.

Supplementary Video 1 | A video showing the left forelimb movement triggered by the photostimulation of a Si mesh. The mesh was attached to the right side of the mouse forelimb primary motor cortex. The stimulation condition was ~ 4 mW for 50 ms. The frame rate is 50 fps with a total time of 490 ms. See more details in **Figs. 4h** and **4i**.

Supplementary Video 2 | Another video showing the left forelimb movement triggered by the photostimulation of a Si mesh. The mesh was attached to the right side of the mouse forelimb primary motor cortex. The stimulation condition was ~ 5 mW for 50 ms. The frame rate is 50 fps with a total time of 490 ms. See more details in **Supplementary Fig. 33a**.

Supplementary Video 3 | A video showing the right forelimb movement triggered by the photostimulation of a Si mesh. The mesh was attached to the left side of the mouse forelimb primary motor cortex. The stimulation condition was ~ 5 mW for 50 ms. The frame rate is 50 fps with a total time of 490 ms. See more details in **Supplementary Fig. 34b**.

Supplementary Video 4 | Another video showing the right forelimb movement triggered by the photostimulation of a Si mesh. The mesh was attached to the left side of the mouse forelimb primary motor cortex. The stimulation condition was ~ 5 mW for 100 ms. The frame rate is 50 fps with a total time of 490 ms. See more details in **Supplementary Fig. 34c**.

References for Supplementary Information

58 Starovoytov, A., Choi, J. & Seung, H. S. Light-directed electrical stimulation of neurons cultured on silicon wafers. *Journal of Neurophysiology* **93**, 1090-1098, doi:10.1152/jn.00836.2004 (2005).

59 Mathieson, K., Loudin, J., Goetz, G., Huie, P., Wang, L., Kamins, T. I., Galambos, L., Smith, R., Harris, J. S., Sher, A. & Palanker, D. Photovoltaic retinal prosthesis with high pixel density. *Nature Photonics* **6**, 391-397, doi:10.1038/nphoton.2012.104 (2012).